SUPPORTING INFORMATION

Contact and Non-Contact Measurement of Electronic Transport in Individual 2D SnS Colloidal Semiconductor Nanocrystals

Adam J. Biacchi*,‡, Son T. Le‡, Brian G. Alberding§, Joseph A. Hagmann‡, Sujitra J. Pookpanratana‡, Edwin J. Heilweil‡, Curt A. Richter‡, and Angela R. Hight Walker*,‡

‡ *Nanoelectronics Group, Engineering Physics Division, National Institute of Standards and Technology (NIST), Gaithersburg, Maryland 20899, United States.*

§ *Remote Sensing Group, Sensor Science Division, National Institute of Standards and Technology (NIST), Gaithersburg, Maryland 20899, United States.*

*E-mail: adam.biacchi@nist.gov, angela.hightwalker@nist.gov

(a) View of armchair bonding

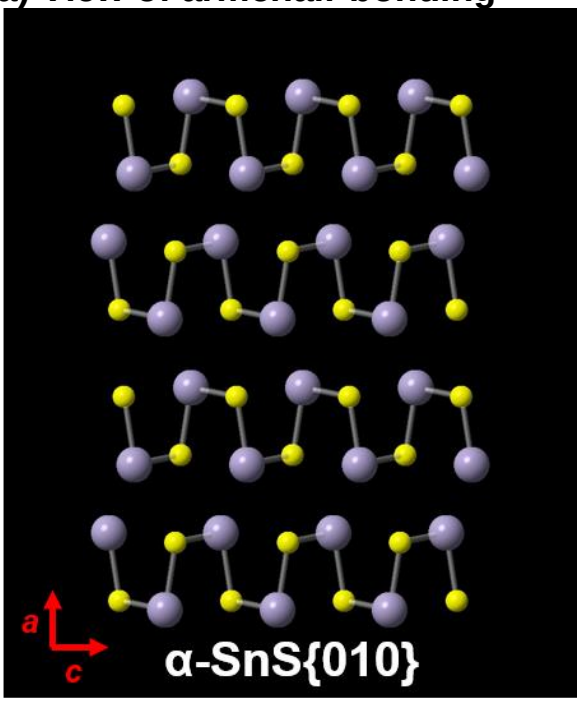

(b) View of zigzag bonding

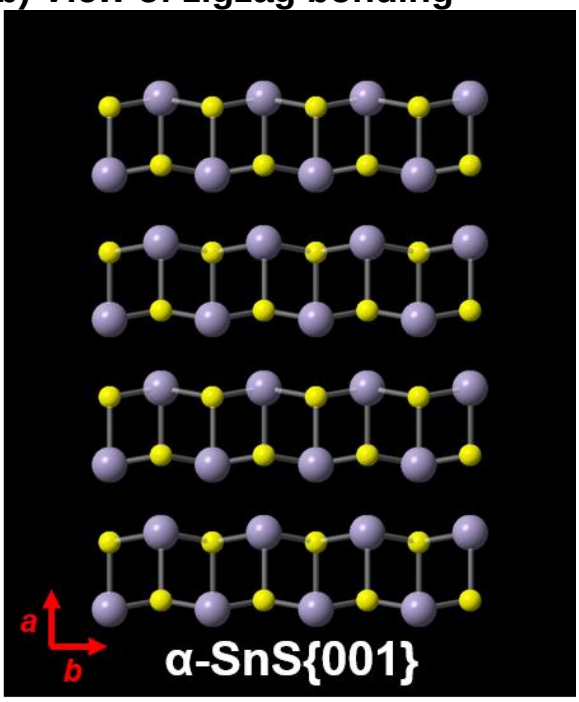

Figure S1. Crystal structure of orthorhombic α-SnS, also known as herzenbergite, (*Pnma*, *a* = 1.118 nm, *b* = 0.398 nm, *c* = 0.433 nm)[1] viewed from (a) the [010] zone axis and (b) the [001] zone axis displaying its layered nature and anisotropic interlayer bonding. Armchair bonding is found in the [001] direction and zigzag bonding is found in the [010] direction. (grey atoms = Sn^{2+}, yellow atoms = S^{2-})

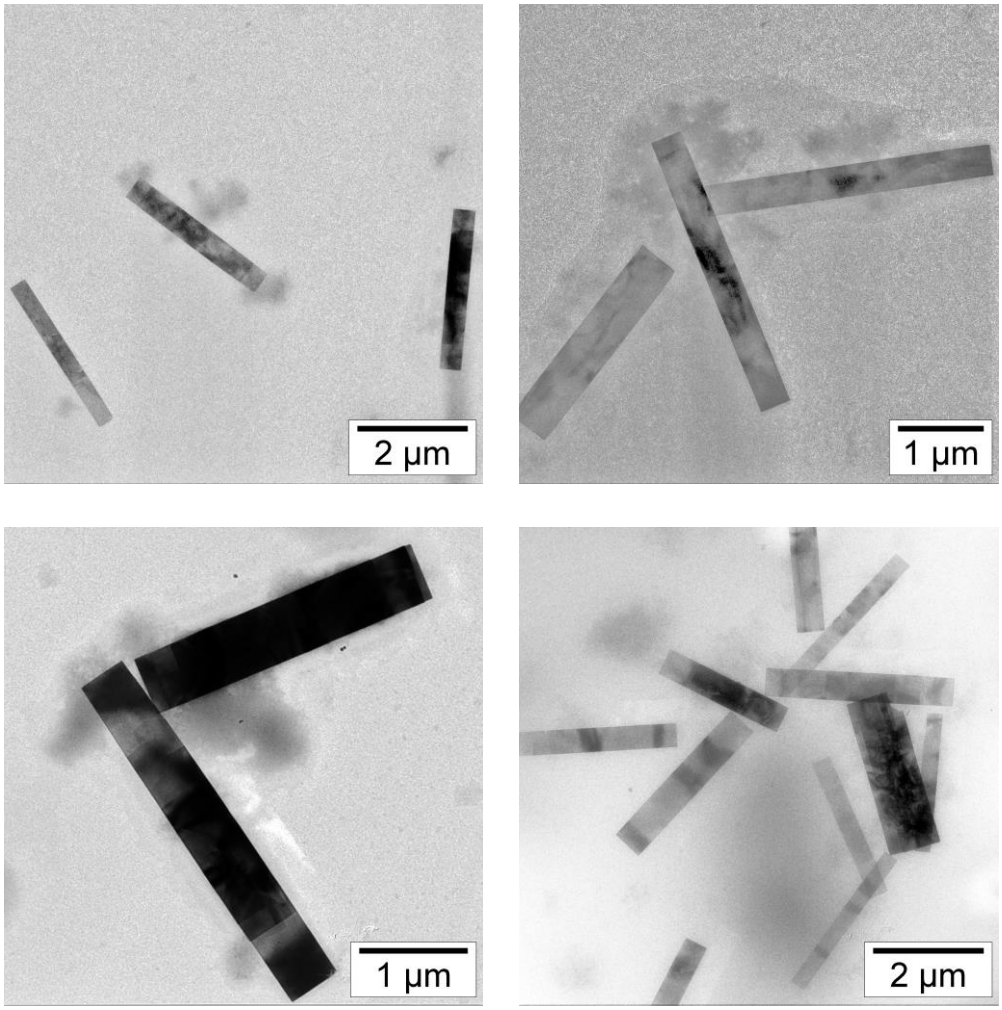

Figure S2. Additional TEM images of SnS nanoribbons.

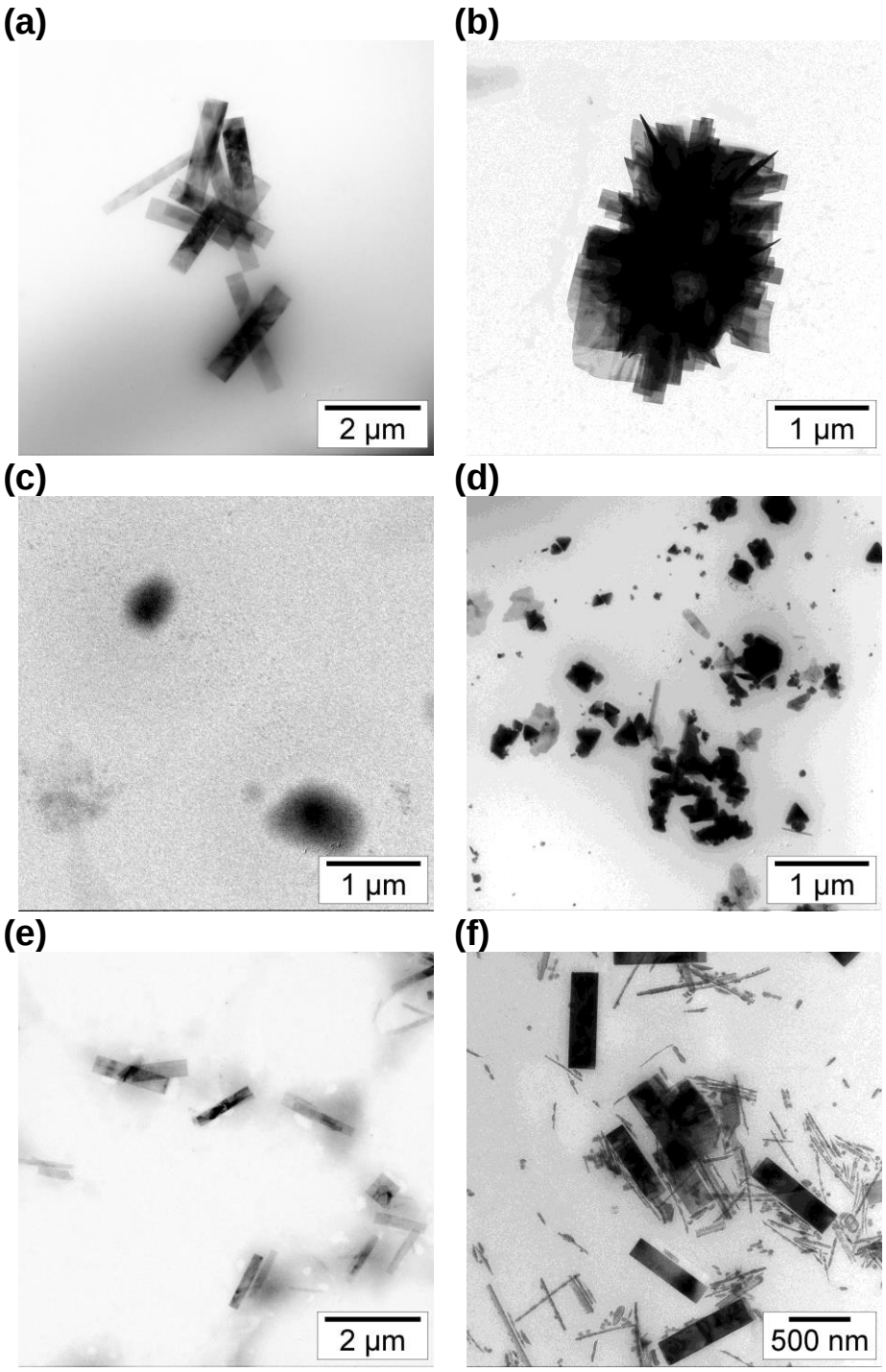

Figure S3. Variation of SnS nanoribbon synthetic conditions. (a) Shorter ribbons form at lower concentration of reagents (0.1 mmol $SnCl_2$ and 0.2 mmol sulfur) but (b) SnS flowers form if the concentration is too low (0.05 mmol $SnCl_2$ and 0.1 mmol sulfur). (c) Only precursor clusters result at 165 °C (438 K) instead of 180 °C (453 K) while (d) a mixture of products form if reagents are hot injected at 200 °C (473 K). (e) Using $SnBr_2$ yields shorter and less monodisperse ribbons, while (f) $Sn(acetate)_2$ produces a mixture of short ribbons and nanowires.

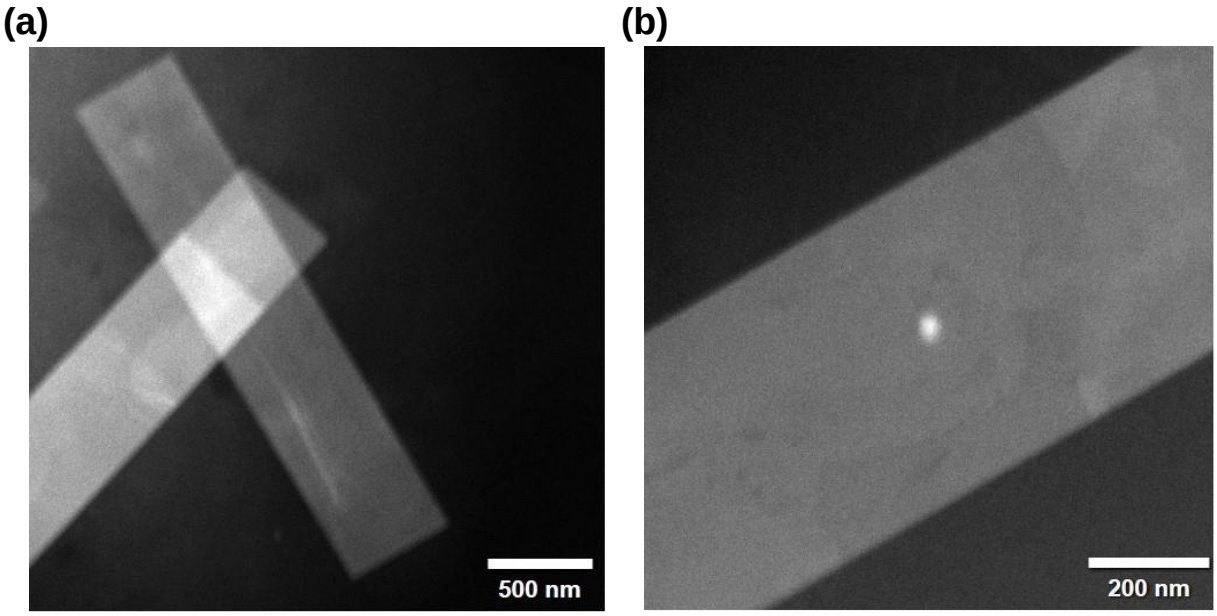

Figure S4. HAADF-STEM images of SnS nanoribbons. The white circle in the center of (b) is due to beam damage.

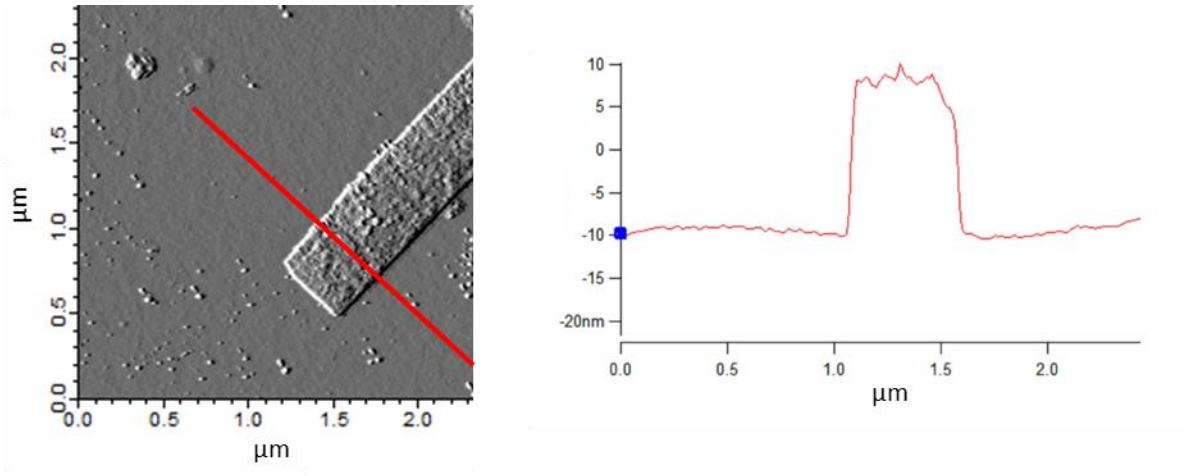

Figure S5. AFM characterization of SnS nanoribbons, indicating their thickness of approximately 17 - 20 nm.

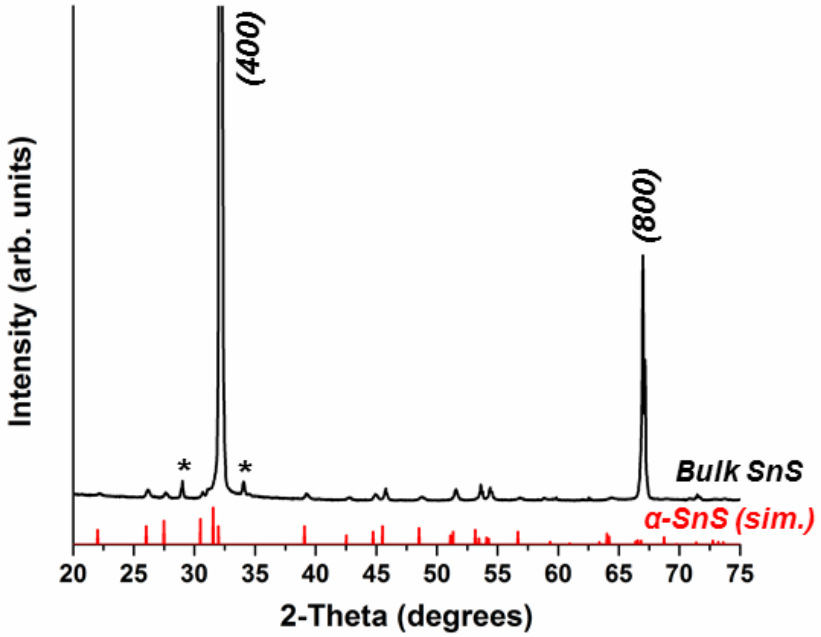

Figure S6. XRD pattern of commercial, bulk herzenbergite SnS (Sigma-Aldrich) compared to the simulated pattern of GeS-type α-SnS (JCPDS card number 73-1859) from Figures 1 and 2 (* = surface oxides).

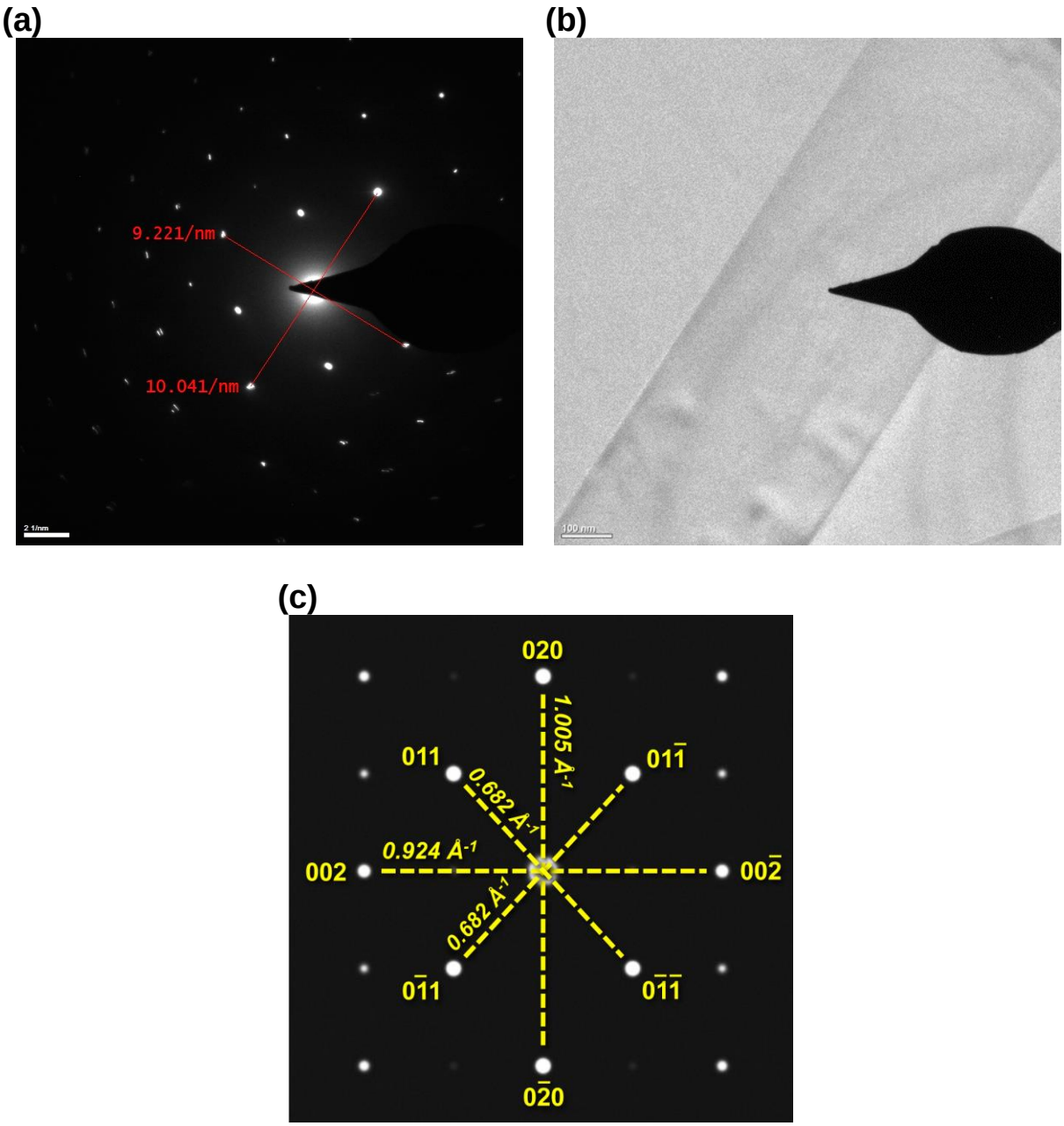

Figure S7. (a) SAED pattern collected from a single SnS nanoribbon and (b) a bright-field TEM image showing the orientation of the nanoribbon producing the diffraction pattern shown in (a). When compared to (c) the simulated electron diffraction pattern for orthorhombic α-SnS(100),[2] the reciprocal space distances between diffraction spots in (a) indicate that the length of the nanoribbon extends in the crystallographic <010> (zigzag) directions, while the width extends in the <001> (armchair) directions.

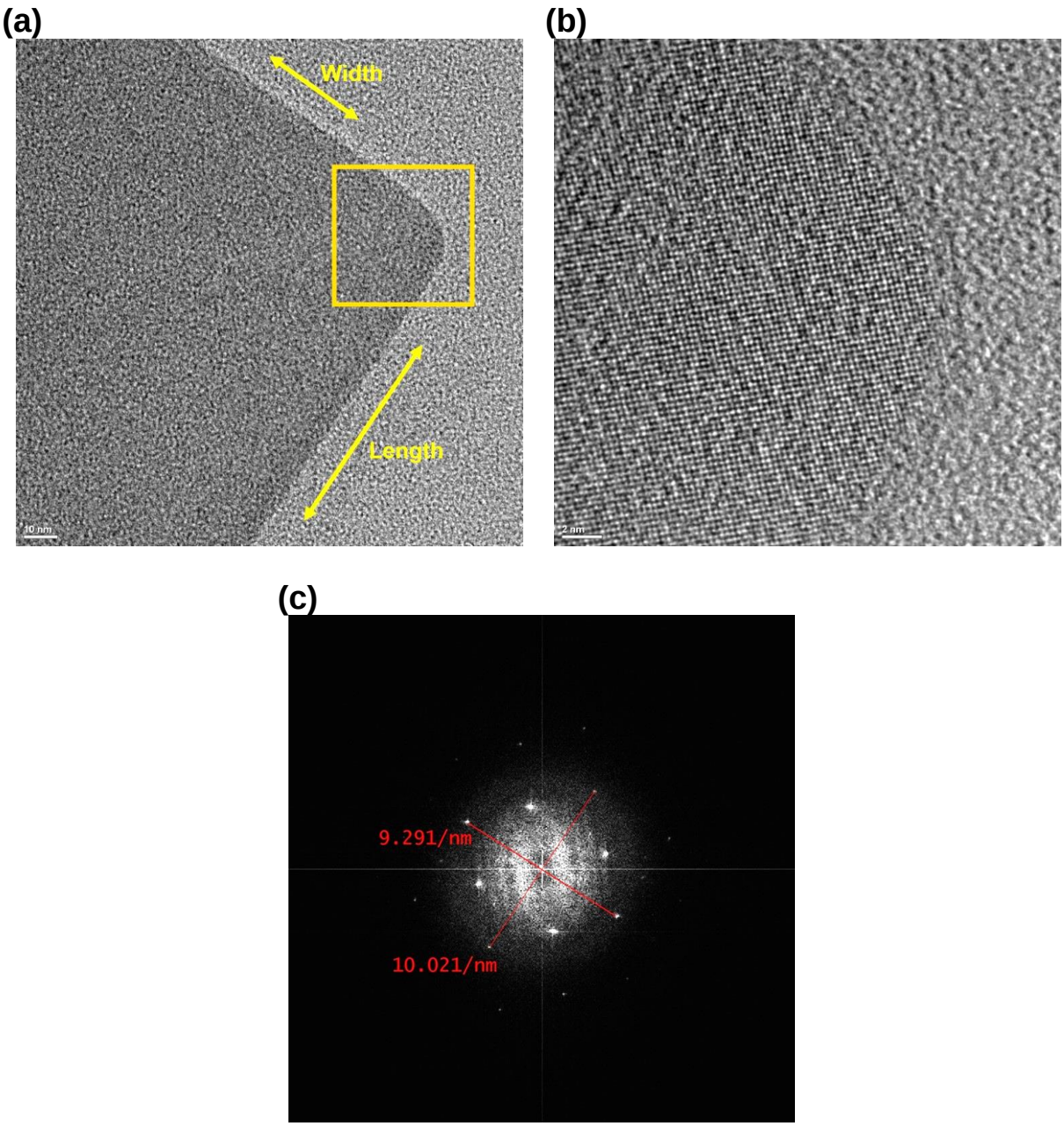

Figure S8. (a) TEM image of a µm-scale SnS nanoribbon and (b) HRTEM image of the highlighted region in (a). (c) The corresponding HRTEM FFT of (b) confirms that the length of the ribbon corresponds to the crystallographic SnS<010> directions (zigzag) and the width to SnS<001> (armchair) when compared to the simulated electron diffraction pattern displayed in Figure S7c.

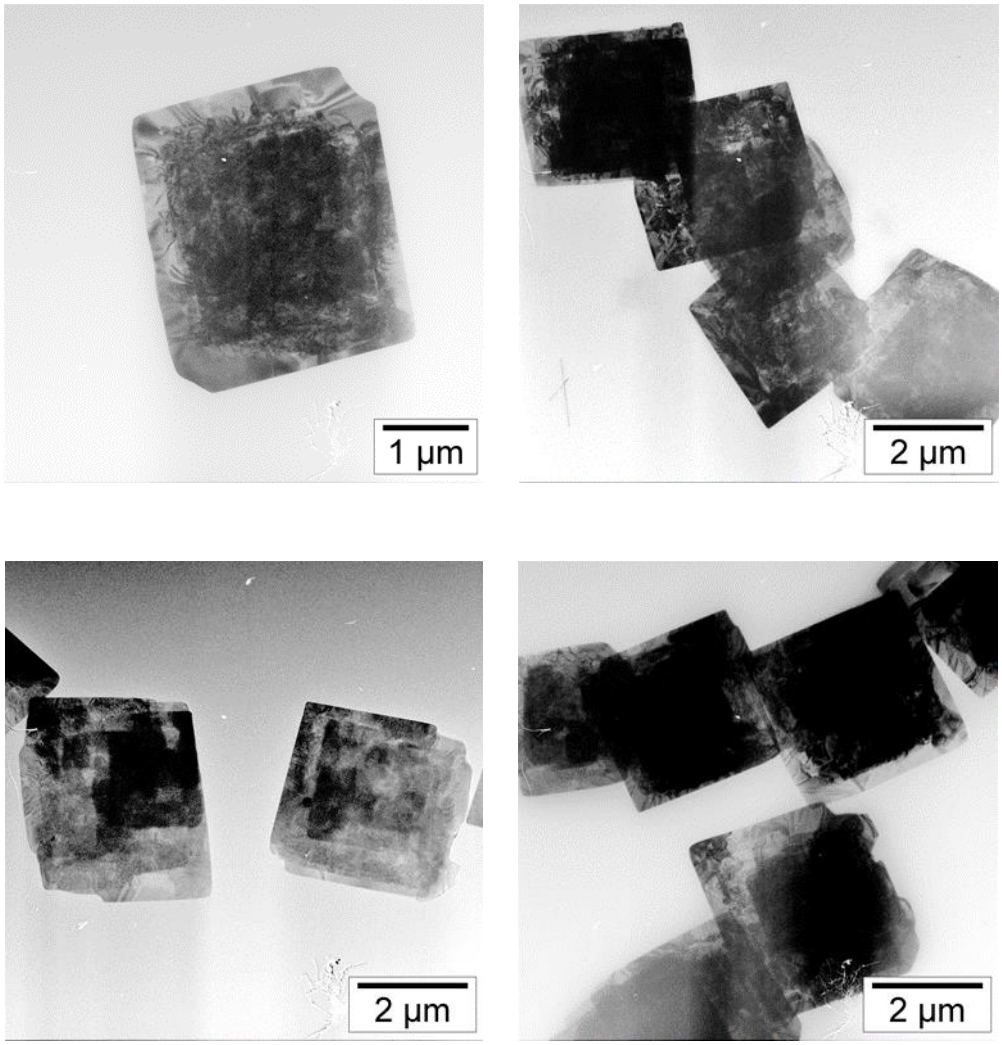

Figure S9. Additional TEM images of SnS square nanosheets.

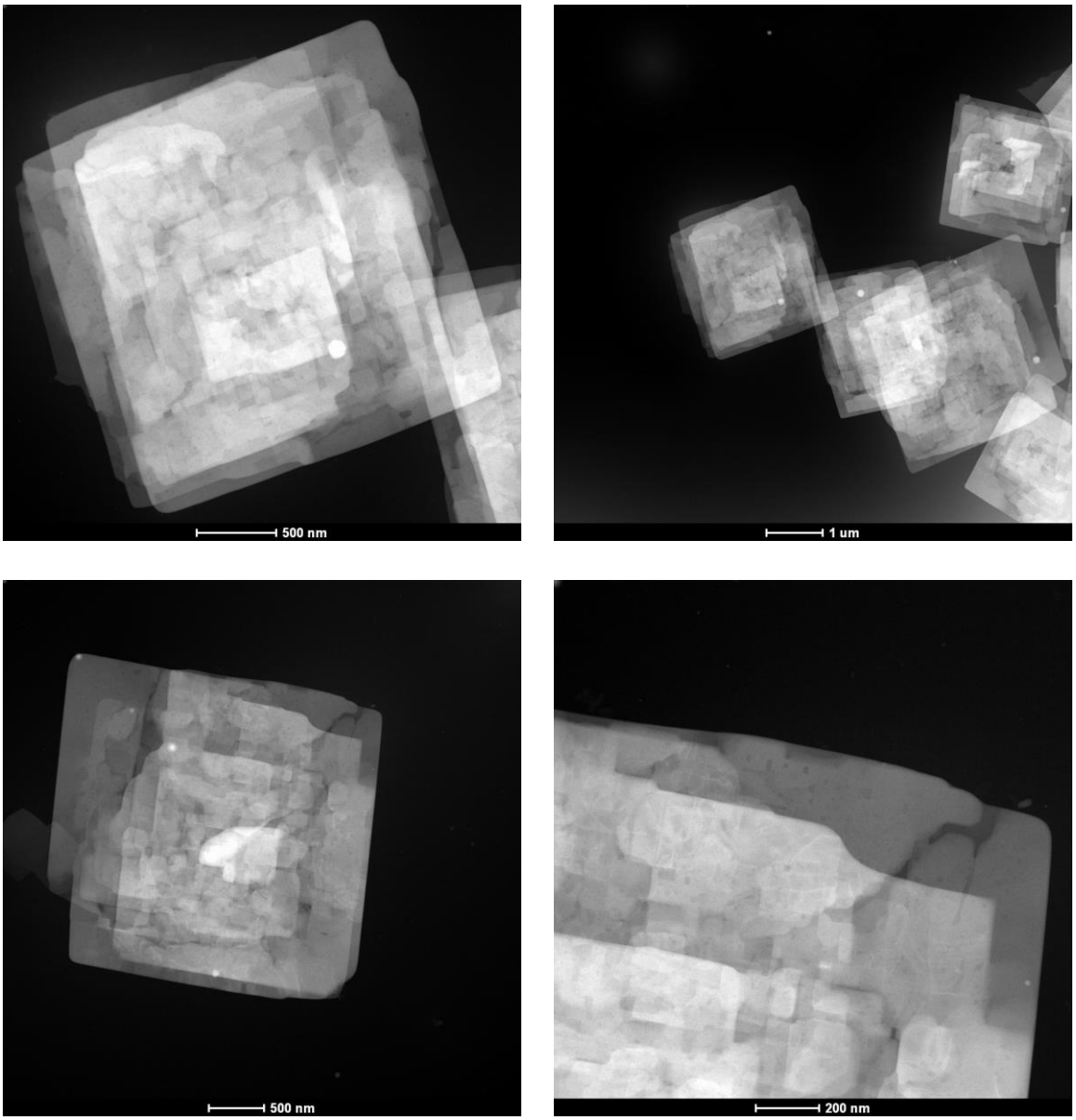

Figure S10. HAADF-STEM images of SnS square nanosheets.

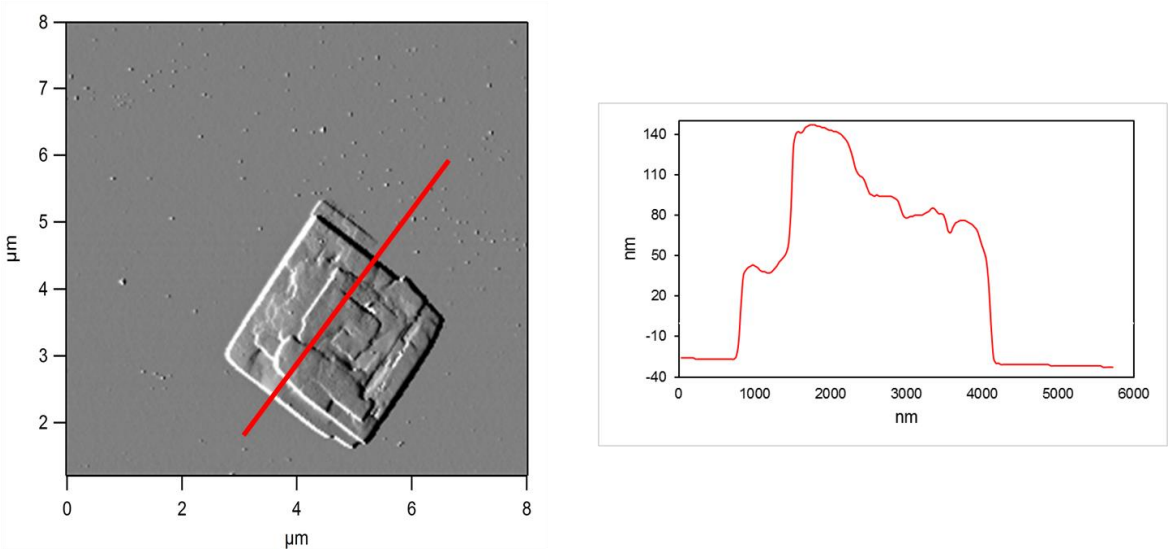

Figure S11. AFM characterization of an SnS square nanosheet, indicating its thickness varies from ≈75 nm to ≈160 nm across the various steps and plateaus of the nanostructure.

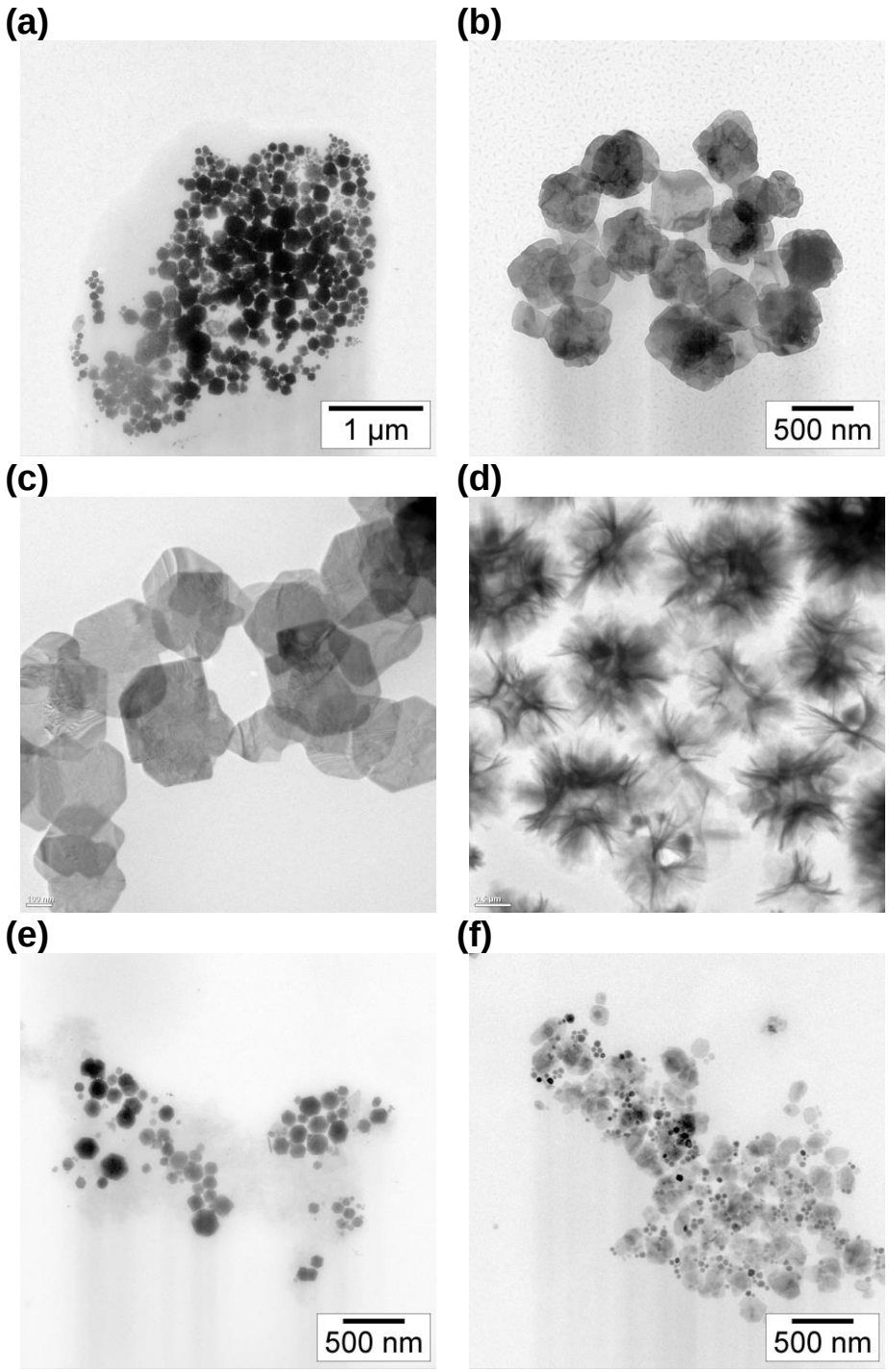

Figure S12. Variation of SnS square nanosheet synthetic conditions. (a) Only polyhedra are obtained without HMDS present, indicating it is essential to the formation of the nanosheets. However, (b) an excess of HMDS (1.25 mL) results in smaller irregular nanosheets, likely due to increased precursor reactivity and corresponding formation kinetics. (c) Small nanosheets form when the Sn:S ratio is increased to 2.5:1, while (d) an excess of sulfur (1:2.5 Sn:S) results in SnS nanoflowers. Replacing $SnCl_4$ with 0.175 mmol (e) $SnBr_4$ yields primarily mixed polyhedra and with (f) $Sn(acetate)_4$ produces a mixture of small rounded sheets and polyhedra.

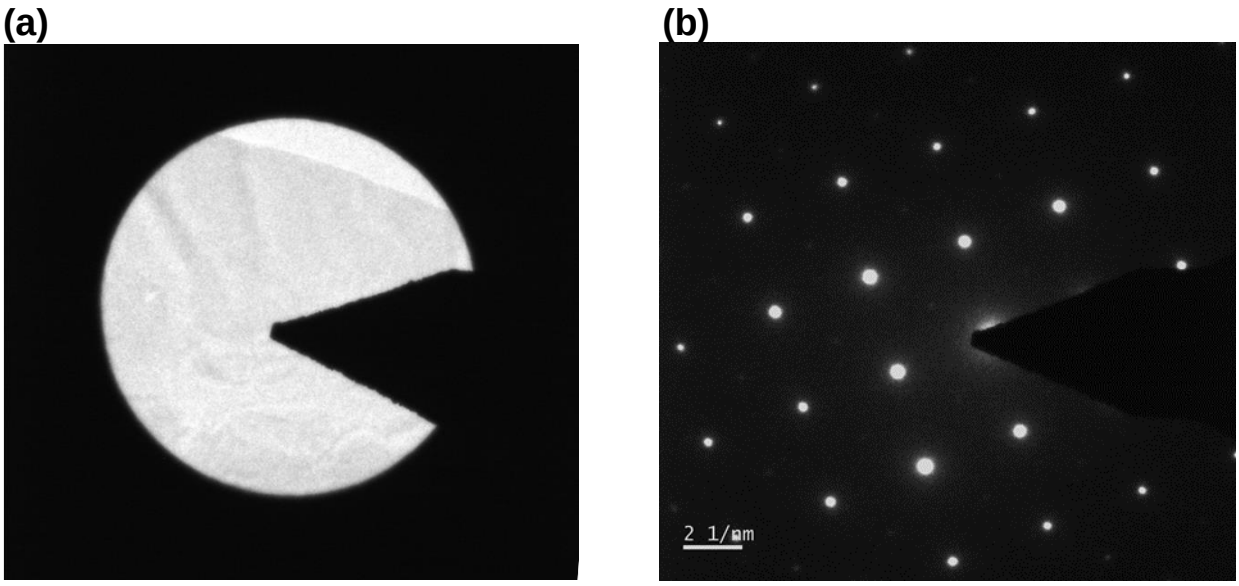

Figure S13. (a) Bright-field TEM image indicating the orientation of the SnS square nanosheet relative to (b) the SnS(100) SAED pattern collected from it, revealing that the edges of the nanosheet correspond to the <010> and <001> directions, while the corners correspond to <011> directions.

(a)

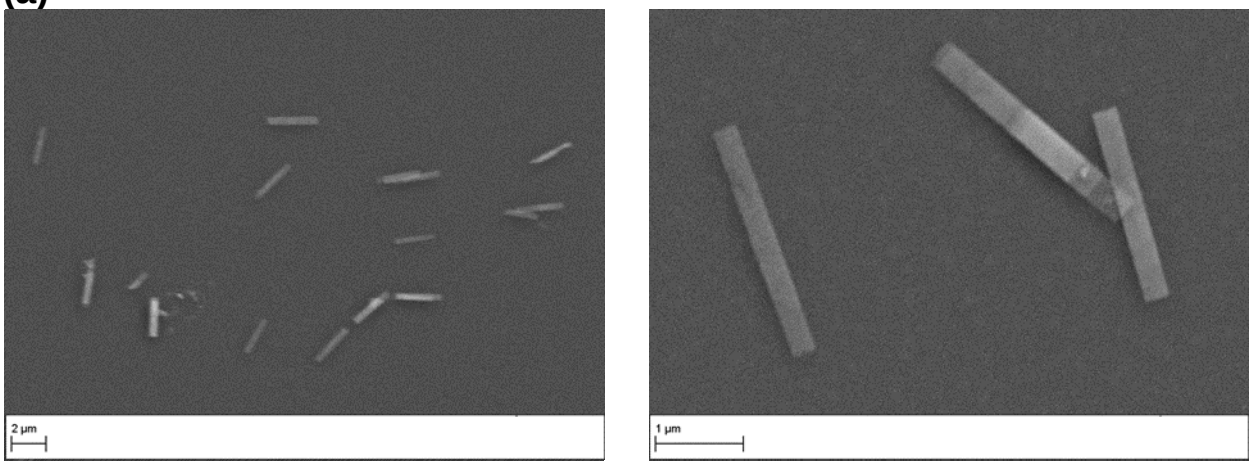

(b)

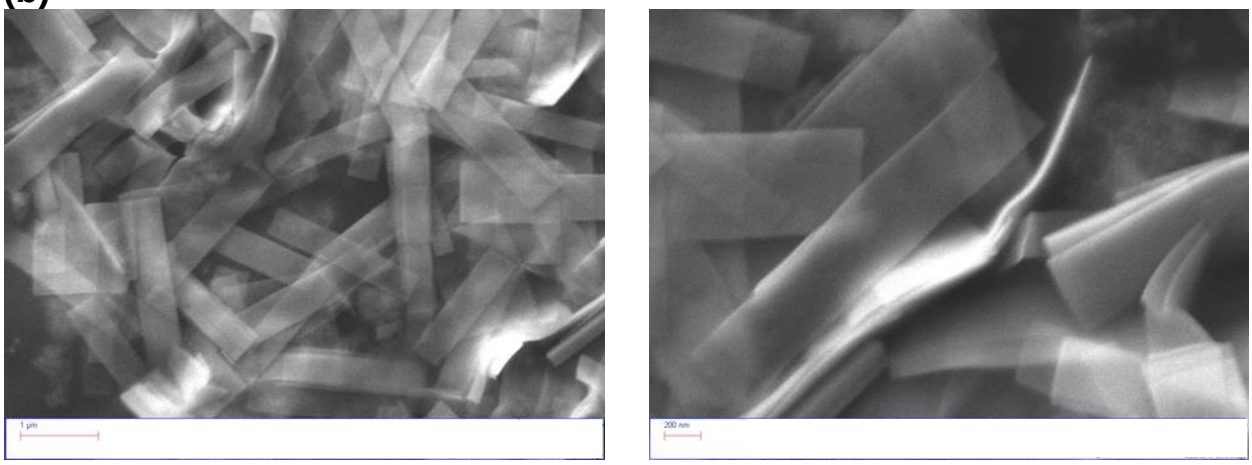

Figure S14. Additional SEM images of (a) dilute and (b) concentrated drop-cast 2D SnS nanoribbons.

(a)

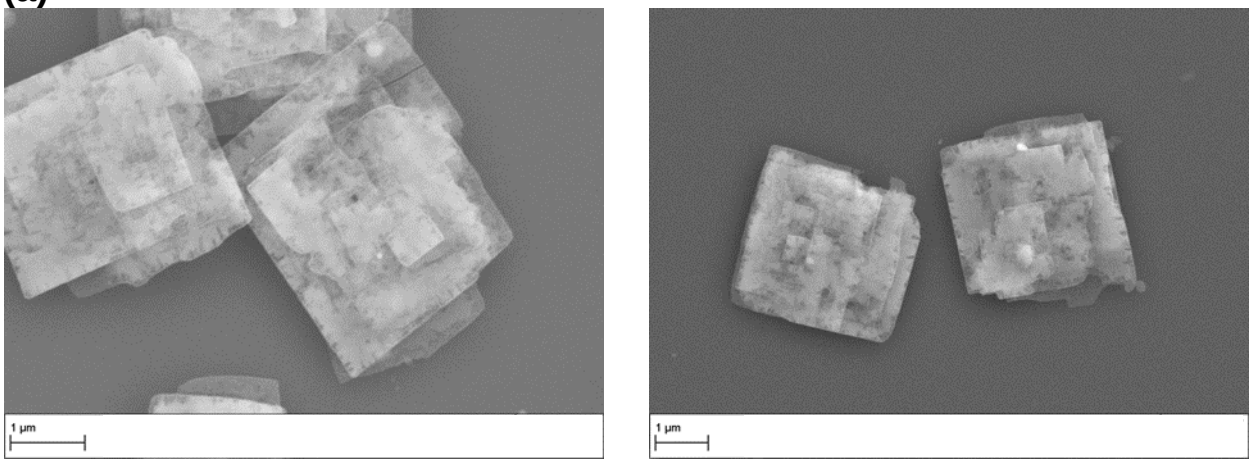

(b)

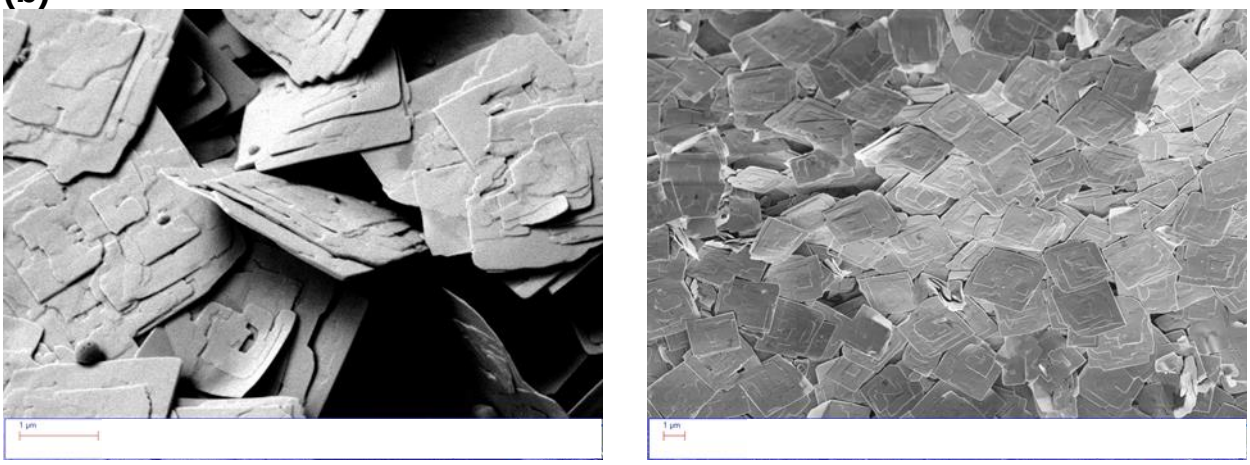

Figure S15. Additional SEM images of (a) dilute and (b) concentrated drop-cast 2D SnS square nanosheets.

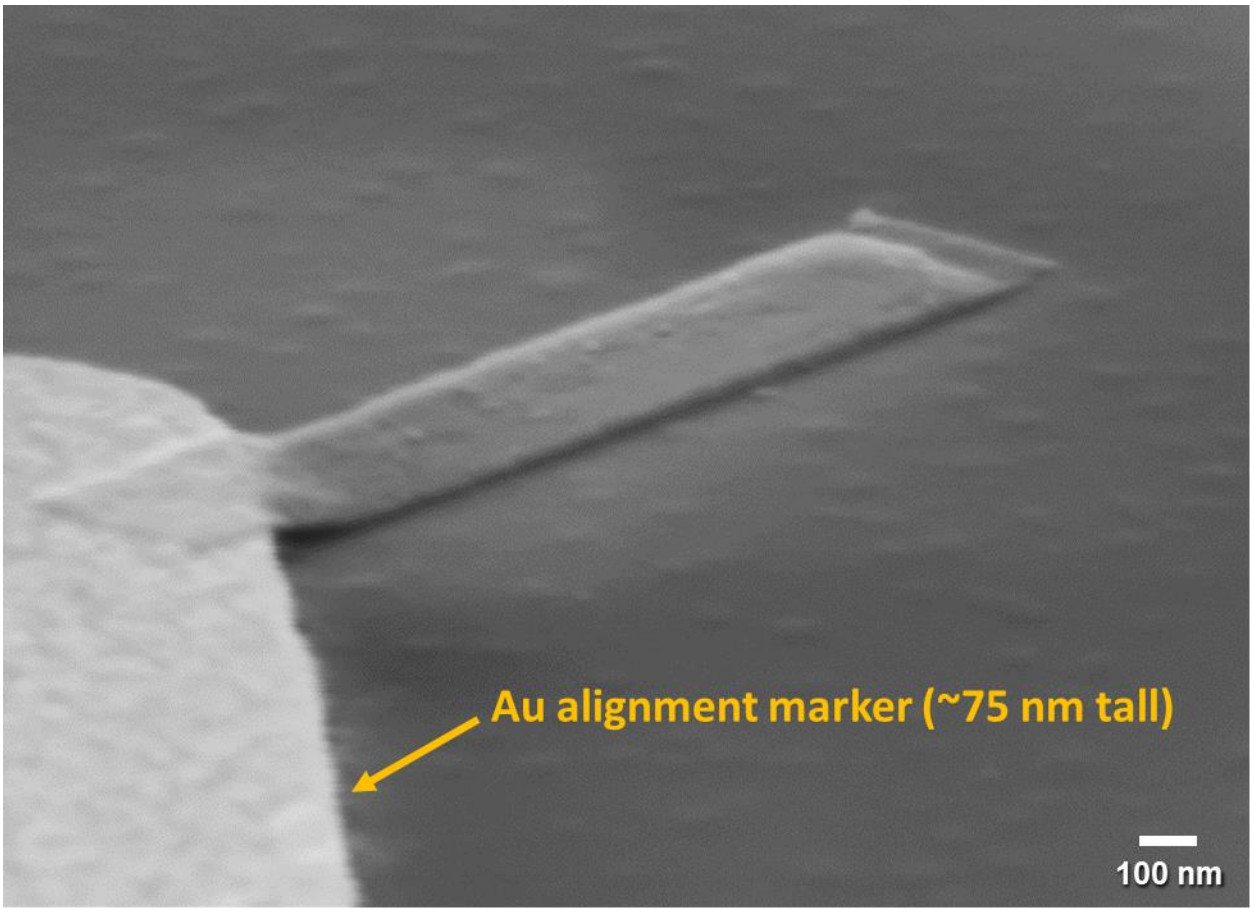

Figure S16. SEM image, taken at a tilt, of an SnS nanoribbon, displaying the elasticity of the nanostructure as it lays astride a ≈75 nm tall fiducial marker on the substrate.

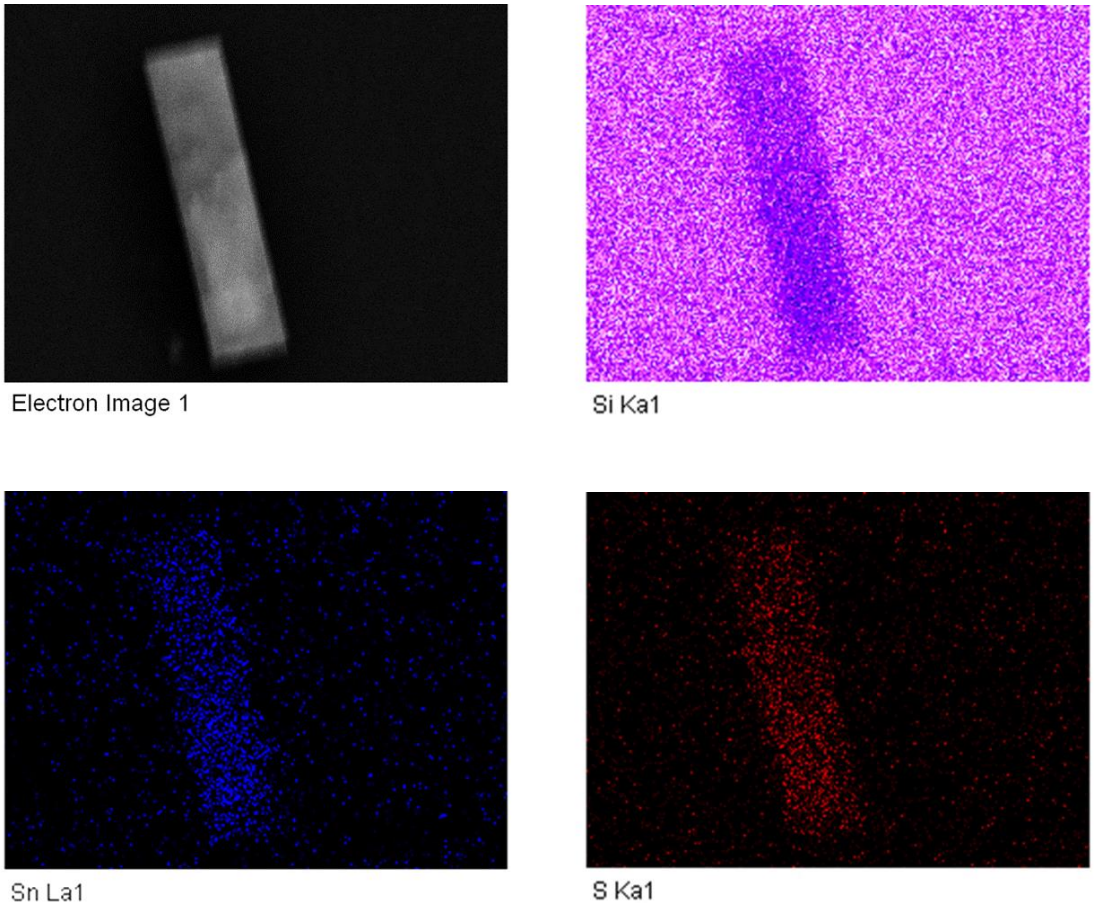

Figure S17. SEM-EDX elemental maps of an individual SnS nanoribbon deposited on an Si substrate, demonstrating a uniform distribution of Sn and S throughout the 2D nanostructure.

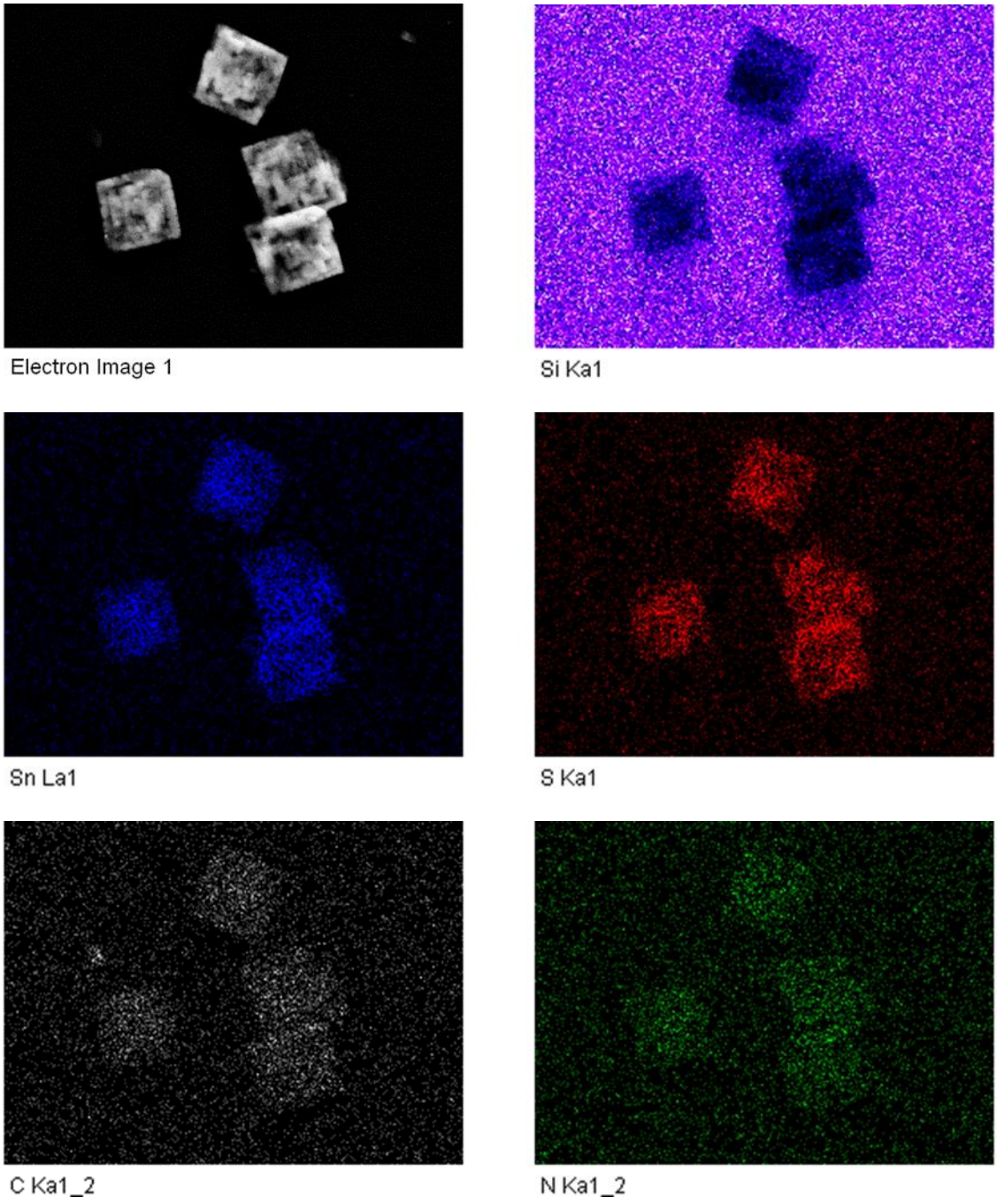

Figure S18. SEM-EDX elemental maps of several SnS square nanosheets deposited on Si, demonstrating a uniform distribution of Sn and S throughout the 2D materials. The presence of C and N detected on the nanocrystals indicates that, despite centrifugal washing, OLAM or other surfactants that provided colloidal stability are still adsorbed to the surface following deposition on the substrate.

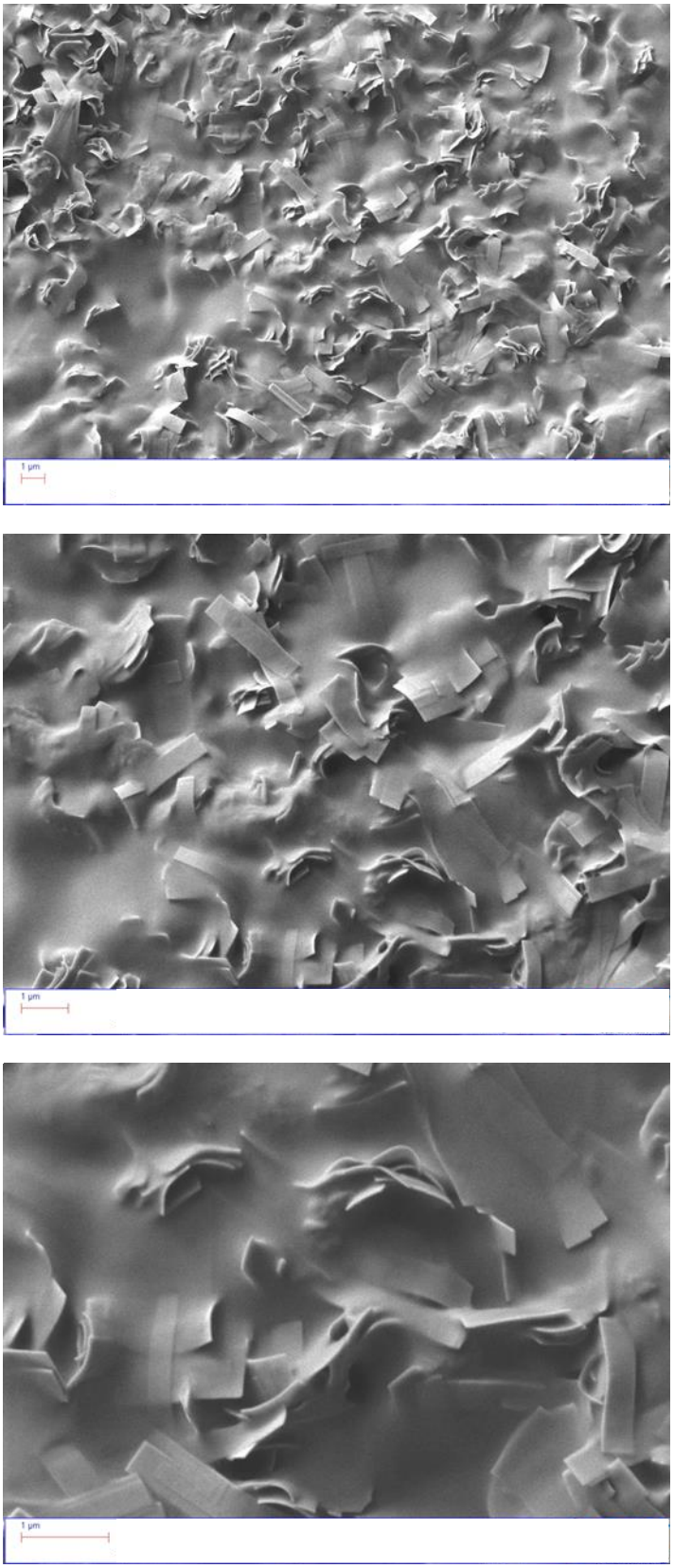

Figure S19. SEM images of a drop-cast SnS nanoribbons without centrifugal washing.

Additional Colloidal SnS FET Device Fabrication Details

We cast a single drop of dilute, centrifugally washed, dispersed nanocrystals in toluene onto a substrate of heavily doped p+Si covered with a 300 nm layer of grown SiO_2 dielectric and an array of photolithographically defined Au fiducial marks. Manipulating the drop concentration allowed for control of the semiconductor density on the substrate. Concentrated drops afford a compact film of SnS, whereas a dilute drop resulted in nanoribbons and square nanosheets distributed across a wide area, appropriate for characterizing or fabricating devices from individual 2D SnS nanocrystals. After drying in air, optical microscopy showed the 2D SnS nanocrystals deposited on the substrate in a random fashion within the circular drop's vicinity. The density of semiconductor nanocrystals on the periphery of the deposition area was unacceptably high for fabrication of single crystal devices due to the "coffee ring effect" (Figures S20a,b,d). However, throughout the interior we found regions of 2D SnS colloidal nanocrystals that had dried from solution with a free proximity of 10 µm or more surrounding them.

After recording the desired device positions relative to the alignment pattern, the substrate was annealed in a tube furnace under an atmosphere of 5 % forming gas at 400 °C (673 K) to remove oleylamine and other organic species from the surface of the 2D SnS. Despite the removal of most surfactant during our initial centrifugal wash, we found that residual molecules adsorbed to the 2D SnS prevented smooth application of our lithographic resist. Fourier-transform infrared (FTIR) spectroscopy confirmed that annealing effectively removed these ligands. As seen in Figure S21, the strong signal of the C-H stretching modes around 2800 cm^{-1} – 3000 cm^{-1}, characteristic of aliphatic hydrocarbons, was no longer present after this thermal treatment. Absorption due to a mixture of alkane, amine, and phosphine moieties located from ~1300 cm^{-1} to 1650 cm^{-1} were also likewise removed by this process. The crystallographic structure of the SnS nanocrystals was preserved during this process, as confirmed by Raman spectroscopy (see Figure S25).

After spin coating a poly(methyl methacrylate) (PMMA) resist, electron beam lithography was used to pattern device contacts on selected individual 2D SnS nanocrystals. Next, the developed area was cleaned and etched of native oxide using a brief hydrofluoric acid wash before proceeding with physical vapor deposition of metal electrodes using an electron-beam evaporator. A Cr adhesion layer (10 nm) was deposited first, followed by an Au noble metal capping layer (70 nm). Liftoff of the resist was achieved in acetone, and images of the resulting device arrays were collected using SEM and optical microscopy (Figures S22-S23).

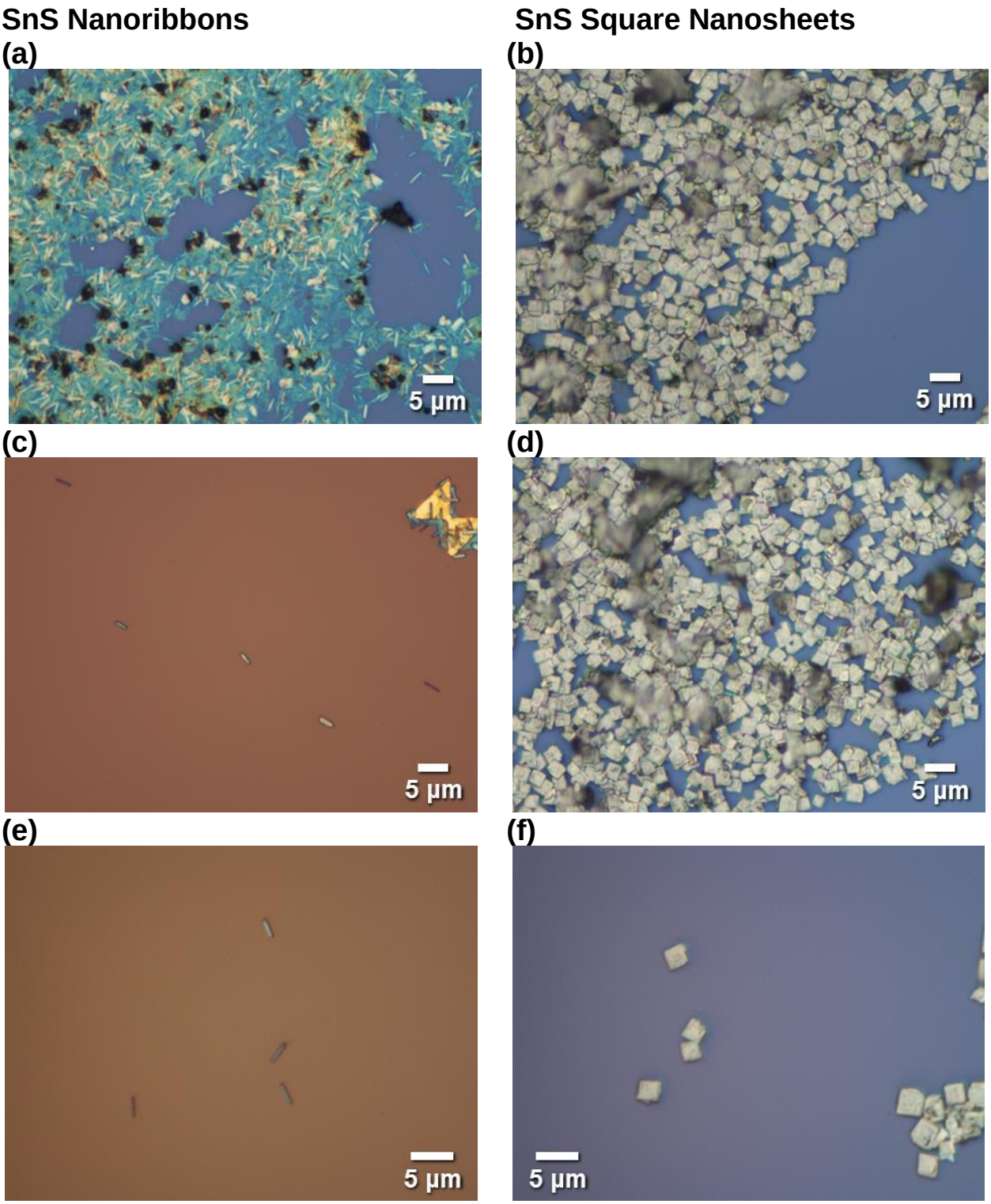

Figure S20. Additional optical microscopy images taken from both concentrated regions (a,b,d) and dilute regions (c,e,f) of drop-cast µm-scale 2D SnS nanoribbons (left column) and square nanosheets (right column).

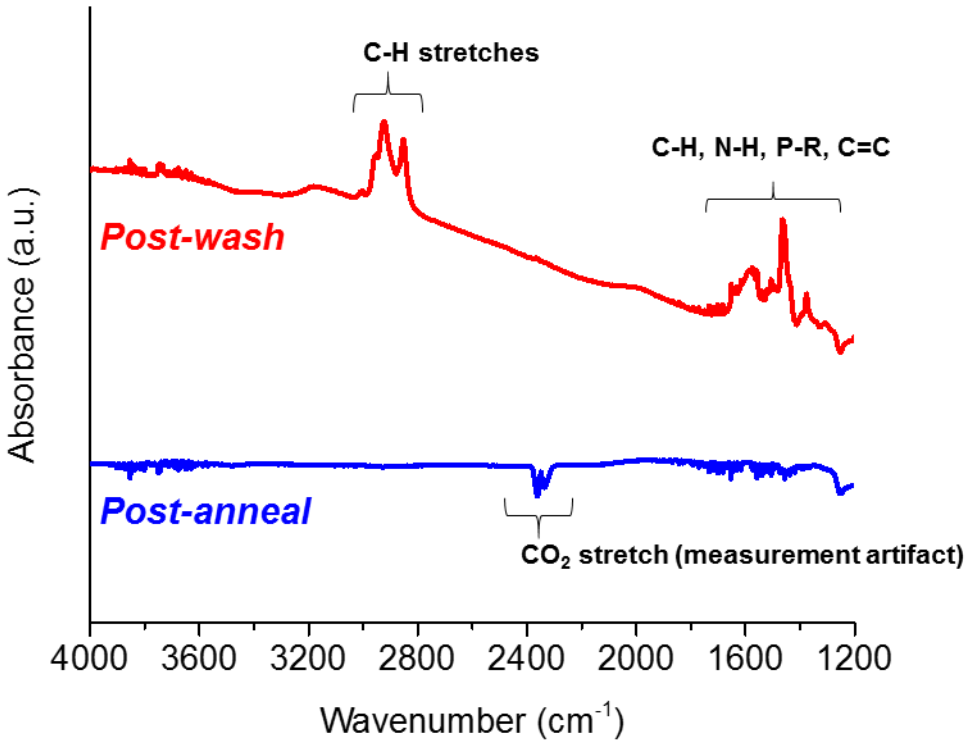

Figure S21. FTIR spectra of SnS nanoribbons prior to annealing (red) and after annealing at 400 °C in forming gas (blue), indicating that organic species present on the surface of the deposited nanocrystals have been removed.

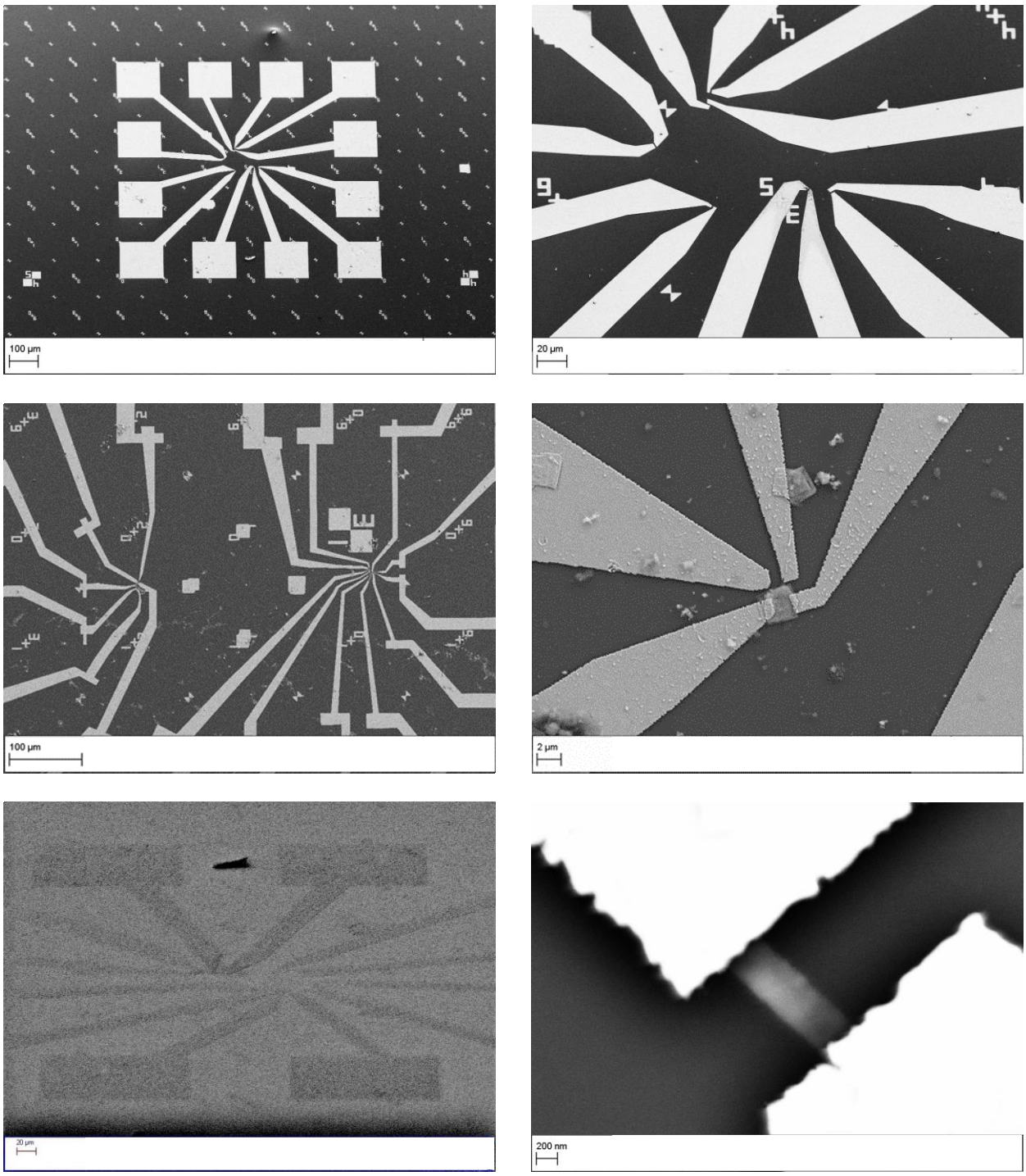

Figure S22. Additional SEM images of fabricated individual SnS nanocrystal device arrays.

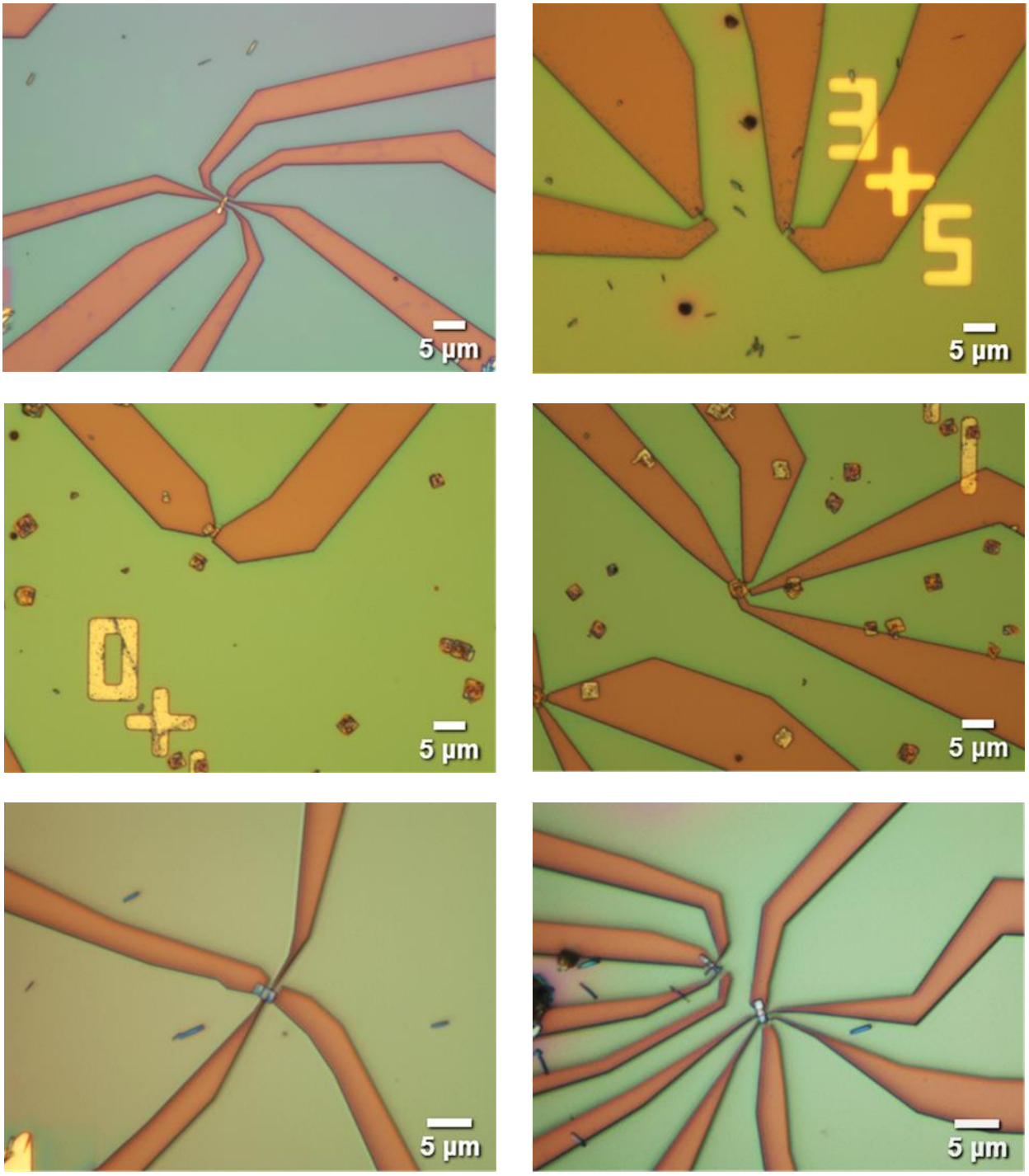

Figure S23. Additional optical images of fabricated individual SnS nanocrystal device arrays.

(a)

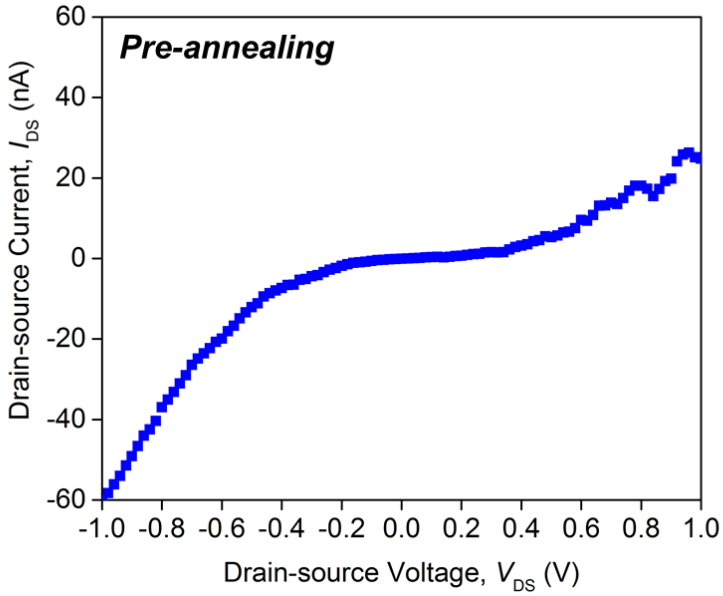

(b)

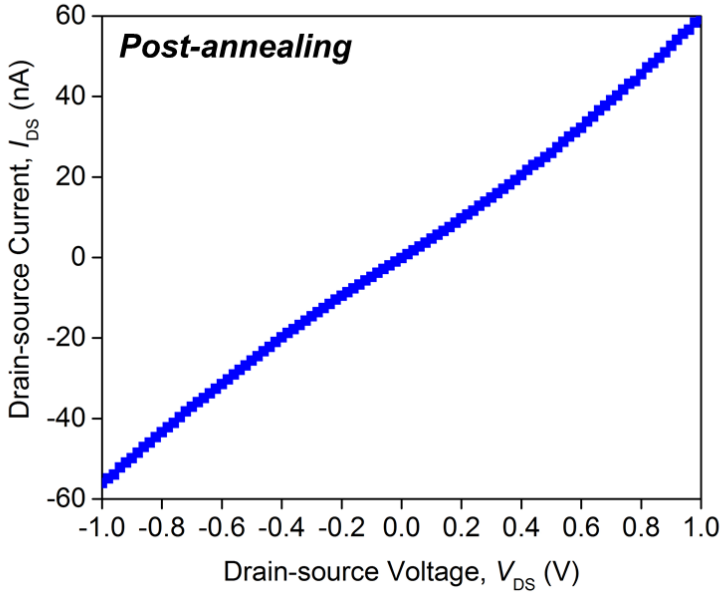

Figure S24. Representative output characteristic at V_{GS} = 0 V (a) before and (b) after annealing of an individual 2D SnS nanocrystal device, indicating a change from Schottky (rectifying) behavior to ohmic behavior.

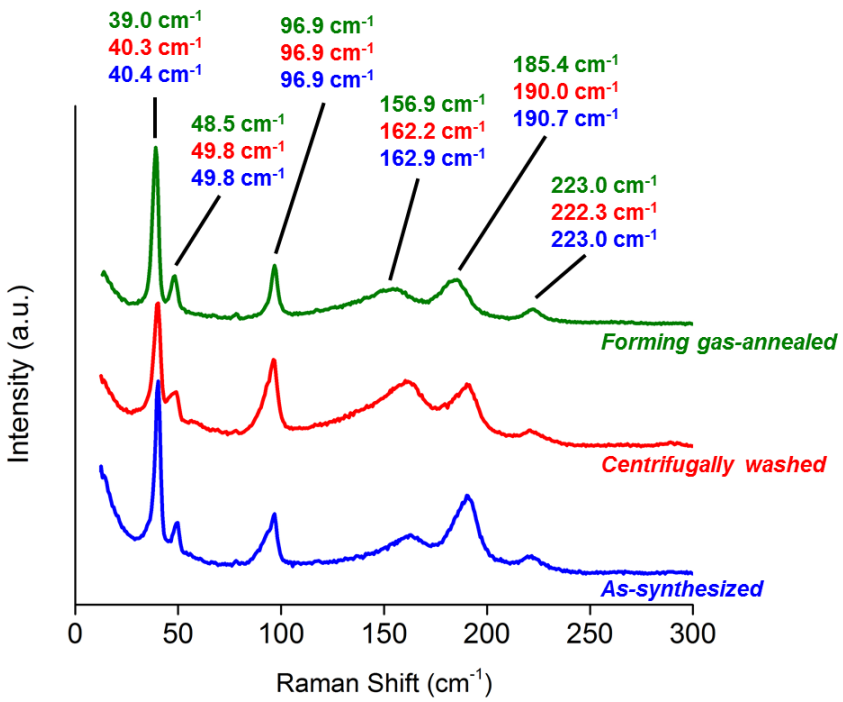

Figure S25. Raman spectra of μm-scale SnS nanoribbons collected as-synthesized, following centrifugal washing, and after the completion of FET devices. Excitation λ = 514 nm. These data indicate that the fidelity of the SnS crystal structure has been maintained throughout the fabrication process

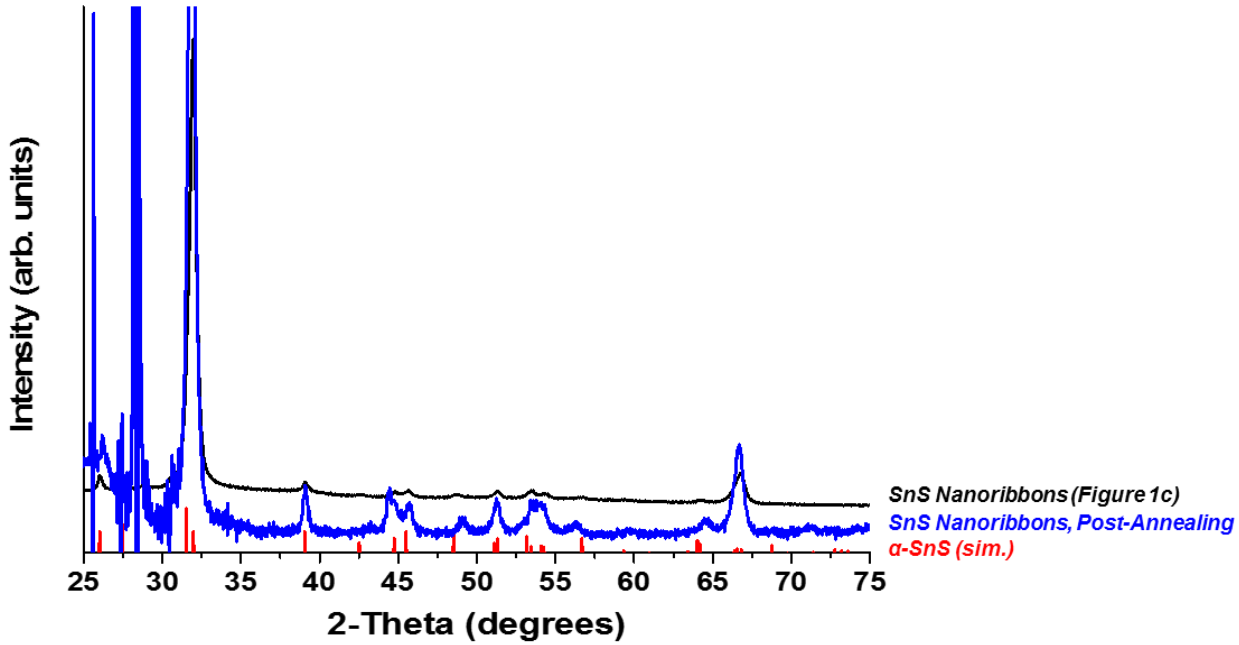

Figure S26. Powder XRD pattern of an ensemble of SnS nanoribbons following annealing at 400 °C in 5% forming gas, indicating that the crystal structure is maintained. The large signals at 25 – 29 °2θ are from the crystalline Si substrate.

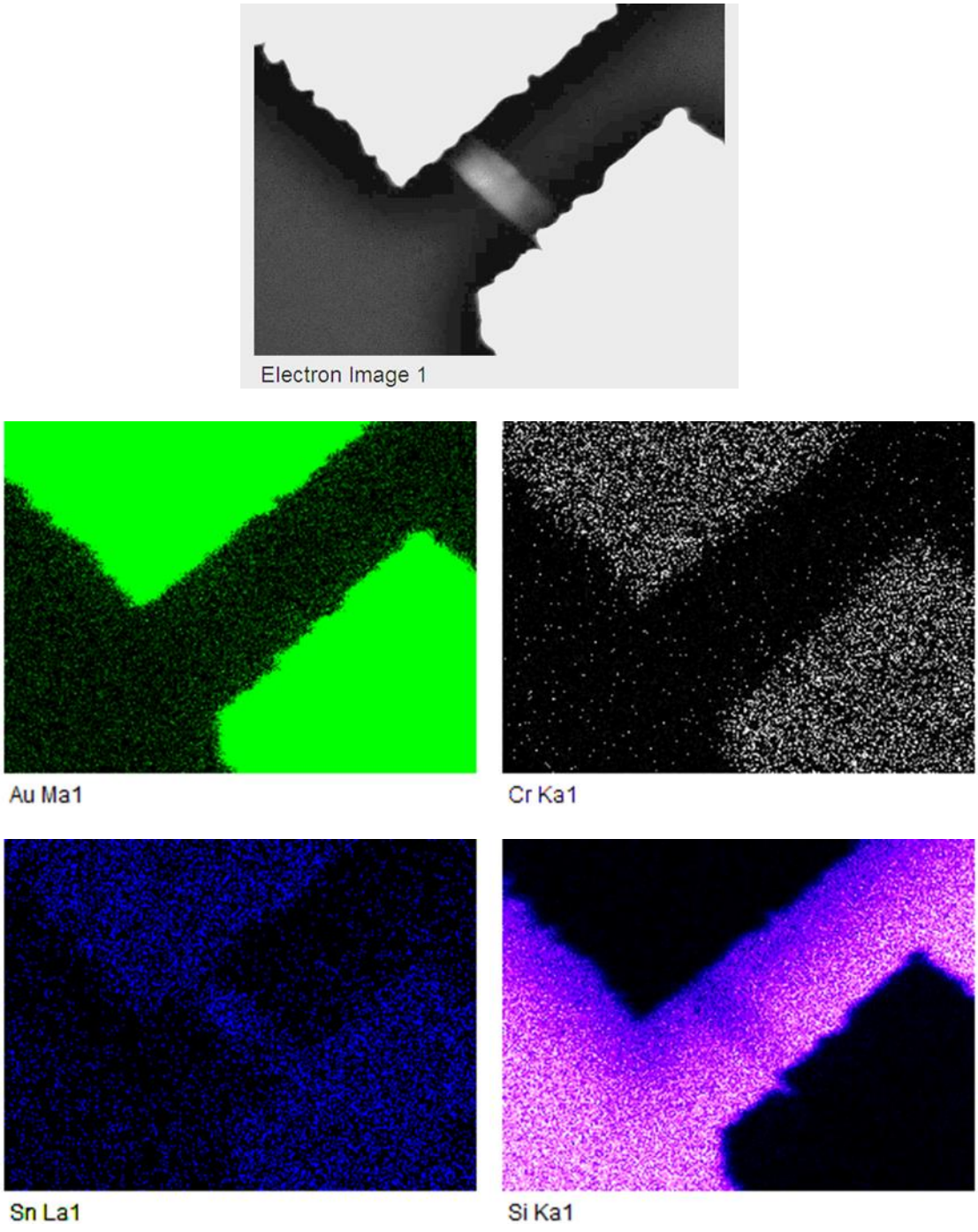

Figure S27. SEM-EDX elemental maps of a fabricated SnS nanoribbon device following annealing, confirming that the device remains intact and indicating that metal from the contacts has not diffused into the semiconductor channel.

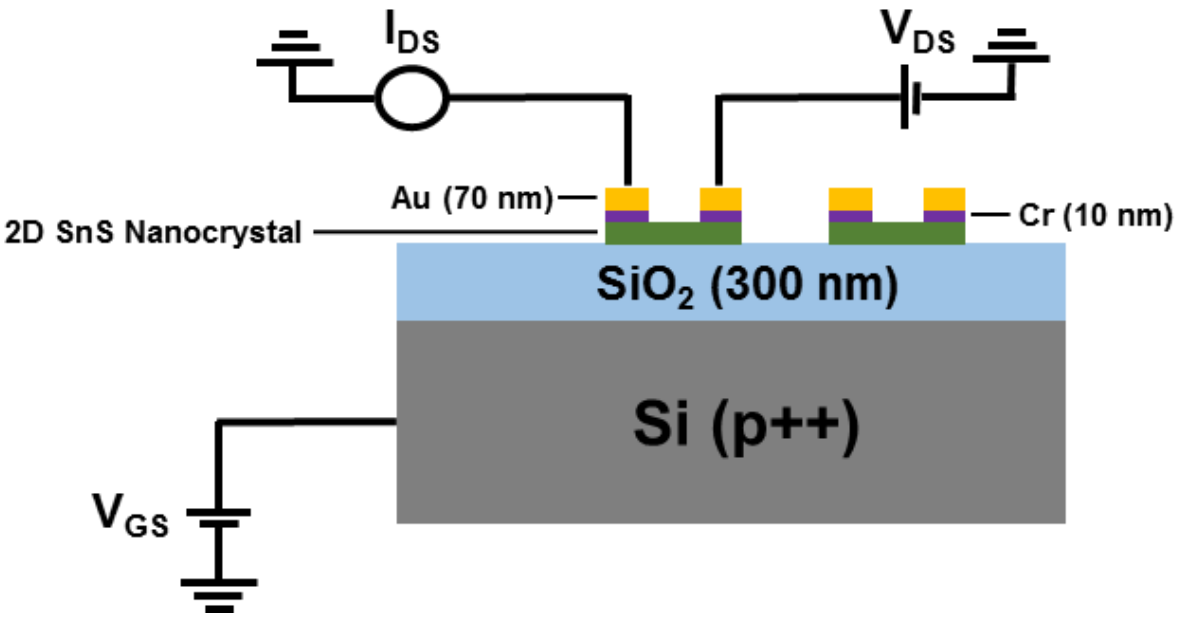

Figure S28. Schematic of individual colloidal 2D SnS nanocrystal-based devices, indicating that they are top-contact, back-gated.

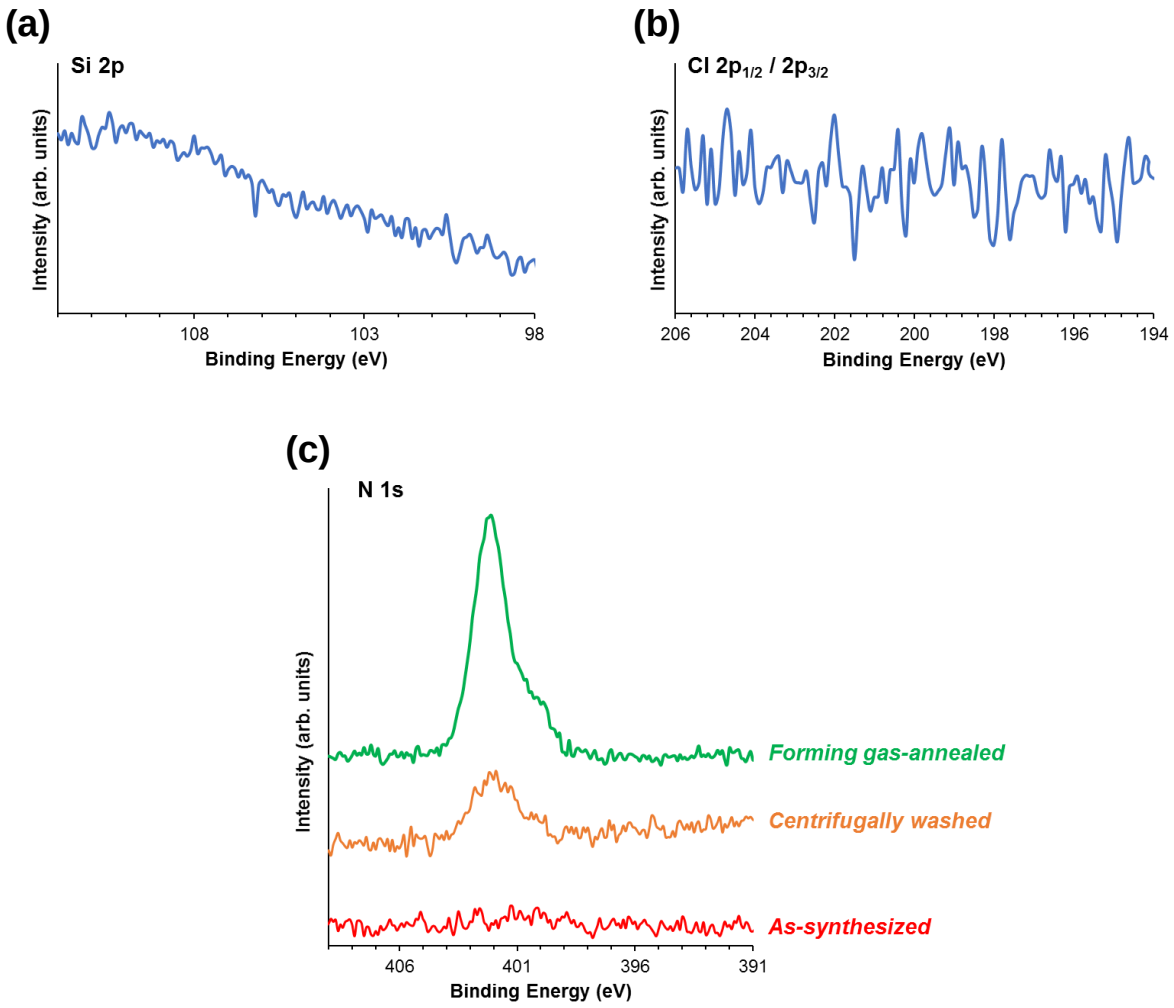

Figure S29. XPS spectra of SnS square nanosheets, centrifugally washed unless otherwise noted. (a) Si 2p region and (b) Cl 2p region, indicating a lack of extrinsic doping by these elements. (c) N 1s region without washing (green), after centrifugal washing (orange), and following annealing in forming gas (red), indicating the removal of OLAM surfactant from the surface.

(a)

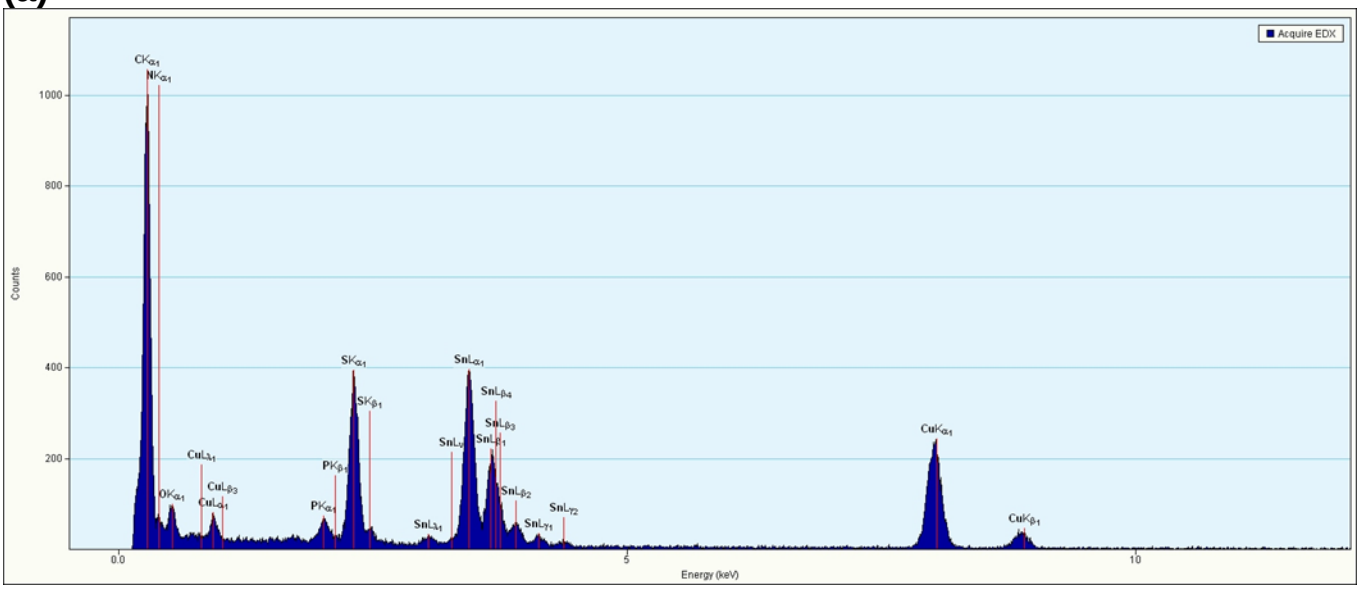

(b)

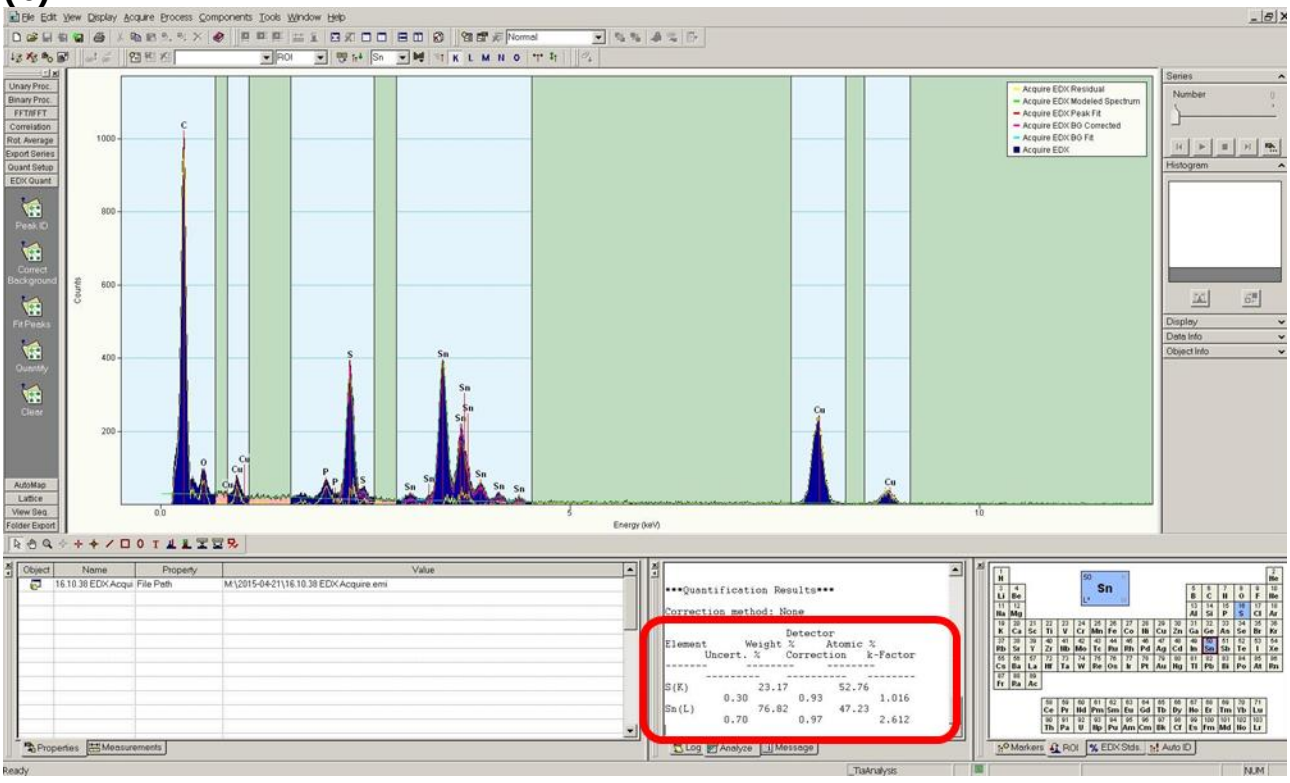

Figure S30. (a)Large-area EDX spectrum and (b) quantitative analysis of SnS nanoribbons, indicating that, stoichiometrically, they are slightly S-heavy (52.76 % S, 47.23 % Sn). Detected C, N, and P are from OLAM and TOP surfactants. Detected Cu is due to the substrate.

(a)

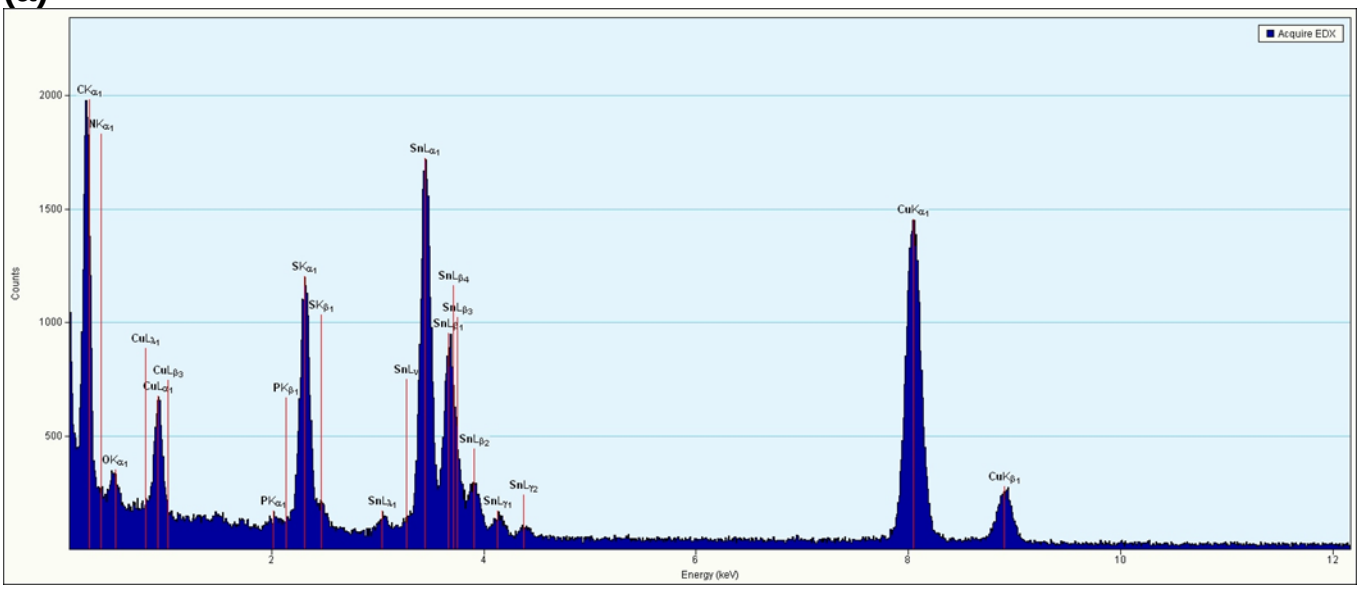

(b)

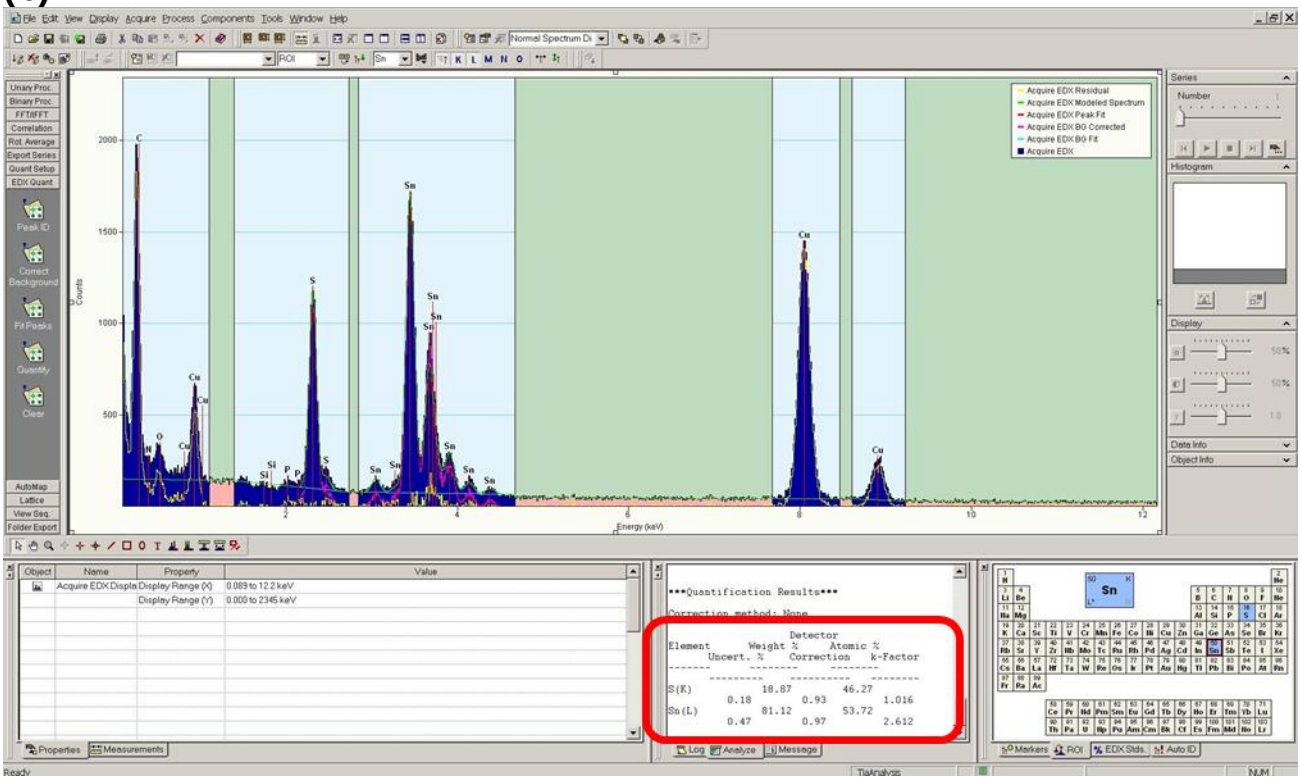

Figure S31. (a) Large-area EDX spectrum and (b) quantitative analysis of SnS square nanosheets, indicating that, stoichiometrically, they are Sn-heavy (46.27 % S, 53.72 % Sn), likely due to the excess Sn^{4+} employed during their synthesis. Detected Cu is due to the substrate.

Additional XPS Analysis Details

To explore the possibility that the relatively low currents displayed by our SnS square nanosheets were due to a thick surface oxide that forms in air, we analyzed the surface composition with XPS. As expected, strong Sn 3d and S 2p peaks were detected (Figure S32). The Sn $3d_{5/2}$ XPS spectrum indicates that an oxide layer is present, as shown by the binding energy feature at 487.1 eV that we ascribed to SnO_x.[3-4] However, the sizeable lower binding energy Sn $3d_{5/2}$ signal located at 485.7 eV corresponds to SnS detected beneath the SnO_x. This implies that the oxide layer must be substantially thinner than the penetration depth of the XPS analysis (8 nm – 10 nm), suggesting the oxide layer at the surface is insufficiently thick to negatively impact performance. Indeed, a thin native oxide passivation layer is potentially advantageous to these semiconductor devices, as they eliminate trap states near the band edges of SnS.[5]

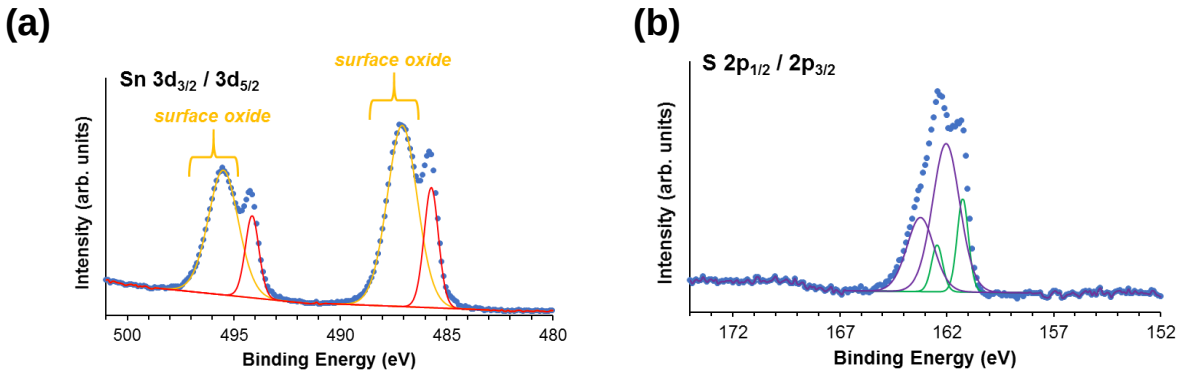

Figure S32. XPS spectra of SnS square nanosheets, centrifugally washed unless otherwise noted. (a) Sn 3d region, indicating the presence of a surface oxide, and (b) S 2p region.

Additional SnS Nanoribbon 4-Point Conductivity Analysis Details

In the case of the nanoribbons, a constant current was forced between the two outermost contacts, which we label 1 and 4, and the differential voltage between the two interior probes, 2 and 3, was measured. For two nanoribbon four-terminal devices, the $I_{DS,1-2}$ - V_{2-3} curves were linear and an average channel resistance of 5.04 x 10^6 Ω was extracted by employing Ohm's law. After establishing the dimensions of the semiconductor channel between contacts 2 and 3 using SEM and optical microscopy, we used the electrical resistivity equation $\rho = \frac{R_{4pt}A}{L}$ where ρ is the resistivity, R_{4pt} is the channel resistance as determined from our four-point measurement, A is the channel area, and L is the channel length, to elucidate the intrinsic material resistivity.

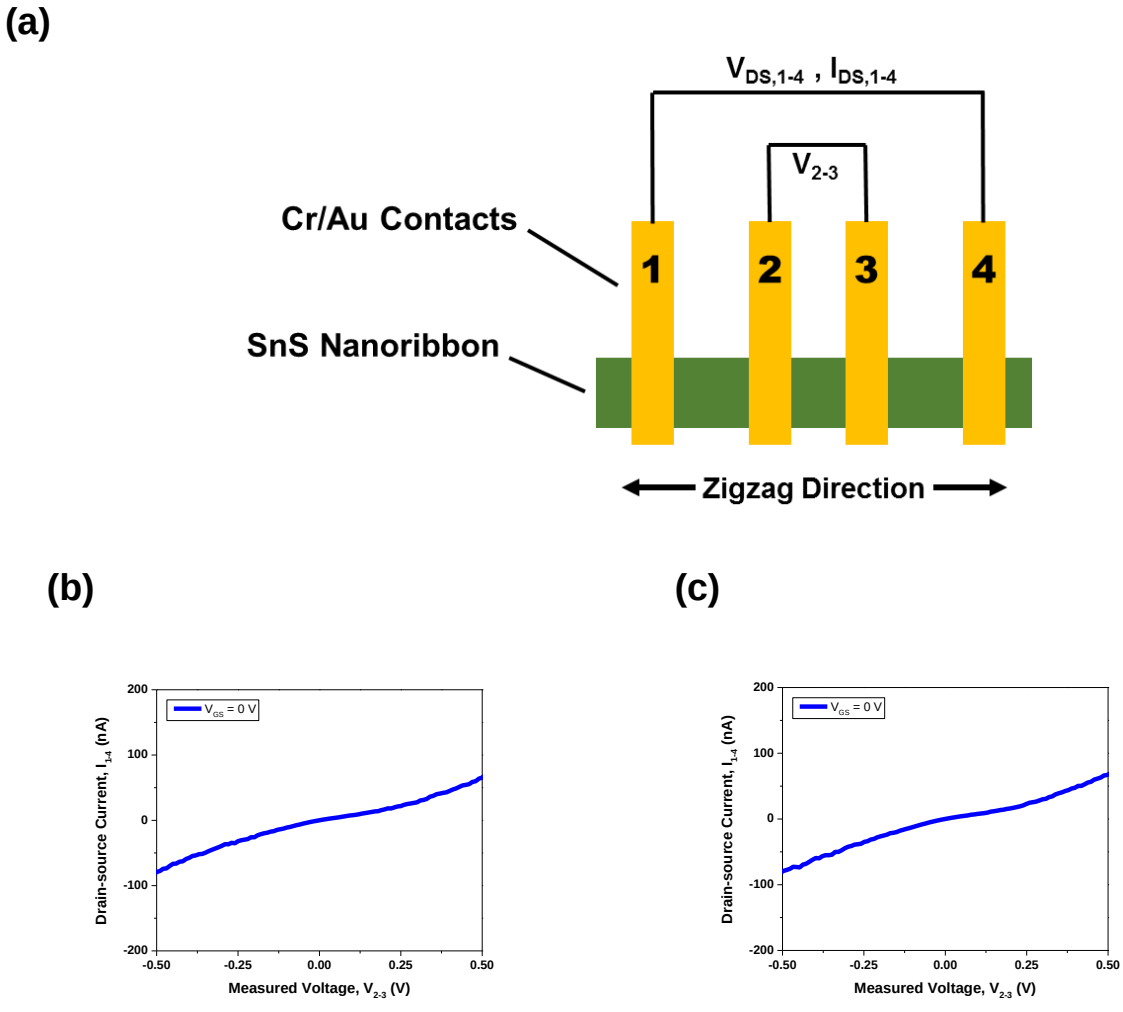

Figure S33. Linear four-point probe conductivity (a) schematic and (b,c) data collected from two SnS nanoribbons.

Additional SnS Square Nanosheet 4-Point Conductivity Analysis Details

Four-point probe analysis of the square nanosheets utilized a van der Pauw configuration, which affords measurements along two directions set off 90° from each other, in this case corresponding to the edges of the square nanocrystals. We found the measured resistances to be highly anisotropic, with an average value of 5.35 x 10^5 Ω in one direction and 8.55 x 10^5 Ω for the orthogonal in-plane direction. The sheet resistance, R_s, was determined by solving the van der Pauw equation,[6] $e^{\frac{-\pi R_X}{R_S}} + e^{\frac{-\pi R_Y}{R_S}} = 1$, where R_x and R_y are the two measured resistances along the edges of our device. Finally, the resistivity of the square nanosheets is calculated by accounting for the thickness of the nanosheet.

(a)

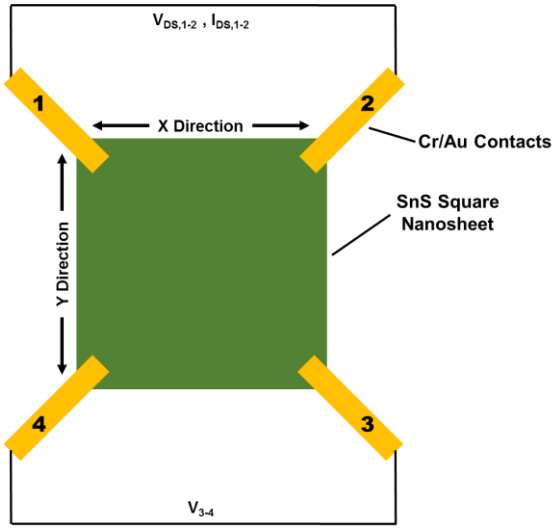

(b) **(c)**

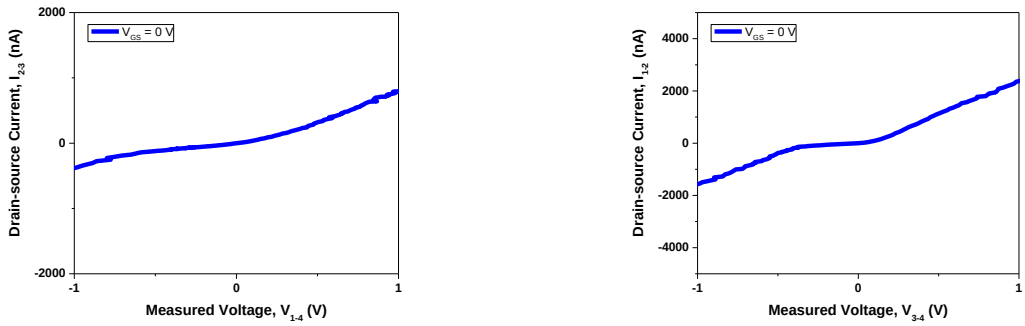

Figure S34. Van der Pauw four-point probe conductivity (a) schematic and (b,c) data collected along two orthogonal directions within the same 2D SnS square nanosheet. The schematic shown in (a) corresponds to the measurements displayed in (c).

Scheme S1. Determination of SnS device field-effect mobility (μ_{FET}).

The field-effect mobility (μ_{FET}) can be calculated from the linear region of a device's transfer characteristic using the equation $\mu_{\mathrm{FET}} = m_{I_{\mathrm{DS}}-V_{\mathrm{GS}}}\left(\frac{L}{W}\right)\left(\frac{1}{V_{\mathrm{DS}}}\right)\left(\frac{1}{C_{\mathrm{ox}}}\right)$, where L and W are the length and width of the channel, V_{DS} is the drain-source voltage, C_{ox} is the gate oxide capacitance per unit area, and $m_{I_{\mathrm{DS}}-V_{\mathrm{GS}}}$ is the slope of the device's linear transfer behavior at low V_{DS}. However, our attempt to extract μ_{FET} at several low V_{DS} values yields discrepant results. For instance, in the case of a two-contact (Cr/Au) SnS nanoribbon FET device fabricated on Si with a 300 nm SiO_2 dielectric (C_{ox} = 1.15 x 10^{-8} F / cm^2) with L = 1270 nm and W = 480 nm:

V_{DS} (V)	$m_{I_{\mathrm{DS}}-V_{\mathrm{GS}}}$ (A / V)	μ_{FET} (cm^2 / V·s)
0.3	4.93 x 10^{-10}	0.38
0.4	1.01 x 10^{-9}	0.58
0.5	1.92 x 10^{-9}	0.88
0.6	2.35 x 10^{-9}	0.90

The inconsistency of μ_{FET} can potentially arise from local non-linearities in the transfer curves, but more likely results from the device resistance associated with the Cr/Au contacts or an interface interaction between SnS and the SiO_2 surface. Unlike Hall mobility[6] and terahertz mobility,[7] these μ_{FET} values correspond to the mobility of the device, rather than the intrinsic mobility of the channel material which, importantly, likely leads to an underestimation of μ relative to the inherent mobility of the semiconductor itself.

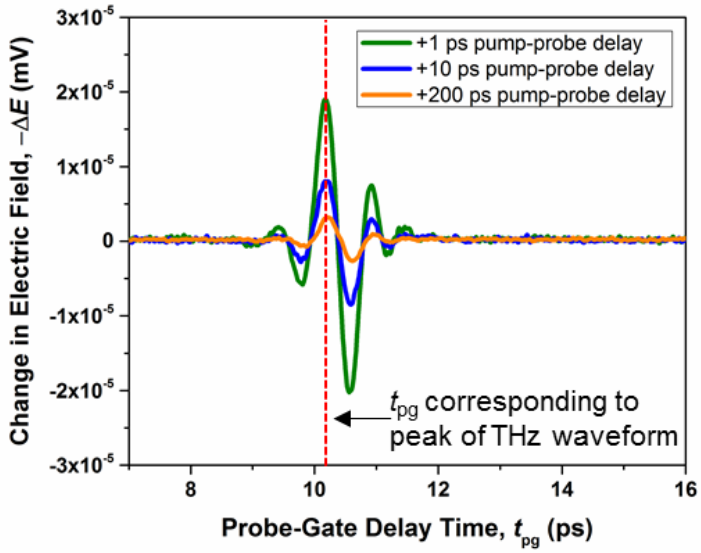

Figure S35. Pumping the deposited 2D SnS with 800 nm excitation induces changes in the terahertz transmission waveform due to increased absorption (larger Δ*E*) by photogenerated free carriers. The magnitude of these changes decreases with increasing pump-probe delay time, t_{pp}. The probe-gate delay time, t_{pg} was set to correspond with the peak of the THz waveform when collecting the t_{pp}-dependent differential transmission $-\Delta E(t_{pp})$.

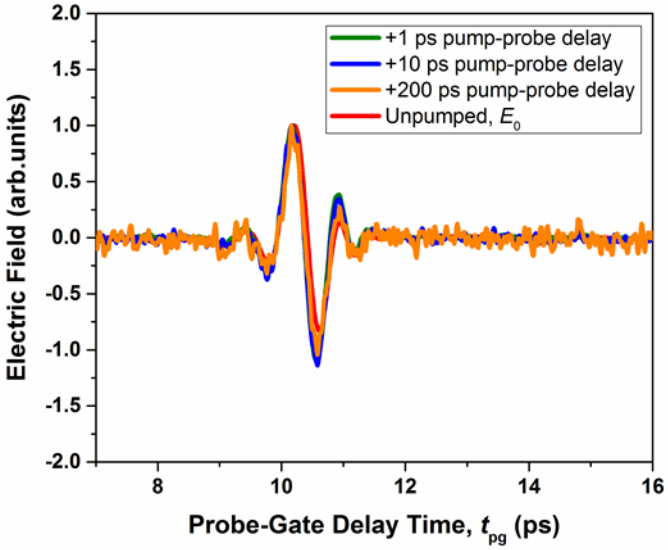

Figure S36. TRTS differential transmission waveforms at several t_{pp} normalized to the signal intensity of the unpumped sample. No observed phase shift is visible, indicating the index of refraction remains constant. (Equation 2 assumes a constant index of refraction of the sample, which was verified by comparing the THz waveforms collected with and without pump beam excitation. In both cases, no discernable phase delay is observed.)

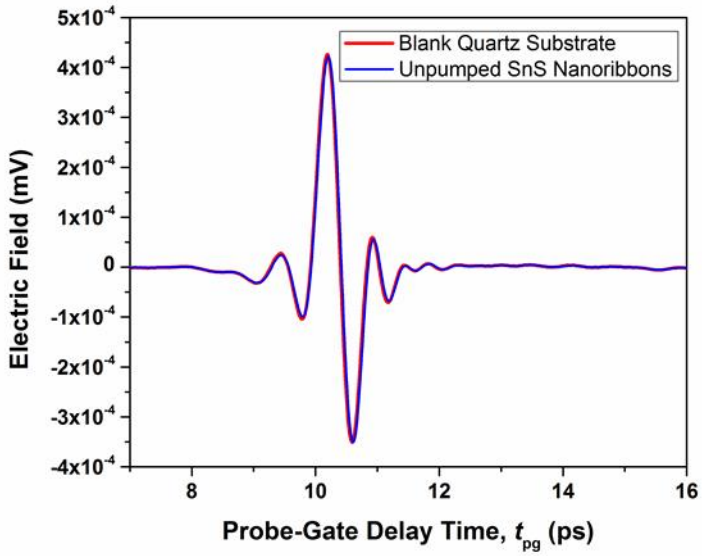

Figure S37. Terahertz time-domain transmission waveforms of SnS nanoribbons deposited on a fused quartz substrate (blue) and the blank substrate (red), demonstrating that the waveform is essentially unchanged without photoexcitation. This indicates that the contribution to TRTS-measured photoconductivity ($\Delta\sigma$) from the inherent, non-photoexcited, SnS free carriers is negligible or smaller than our detection limit. The pump-generated photoconductivity, $\Delta\sigma(t_{pp})$, can be assumed $\approx \sigma(t_{pp})$ if the detected conductivity contribution of the non-photoexcited sample is very low.

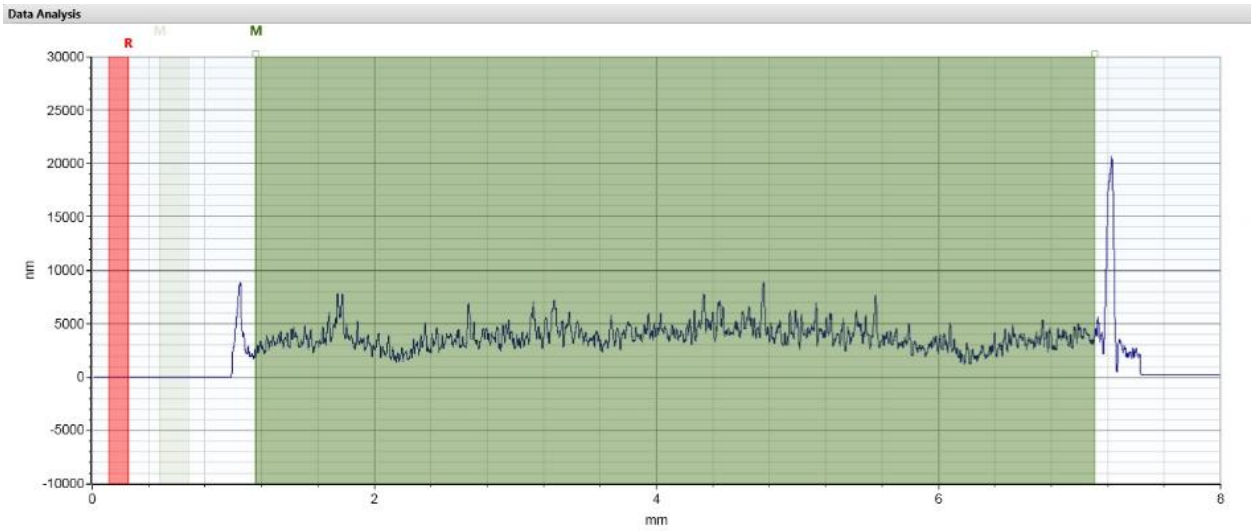

Figure S38. Contact profilometer characterization of a film of SnS nanoribbons drop-cast on a fused quartz substrate, indicating that the average thickness is 3.78 µm.

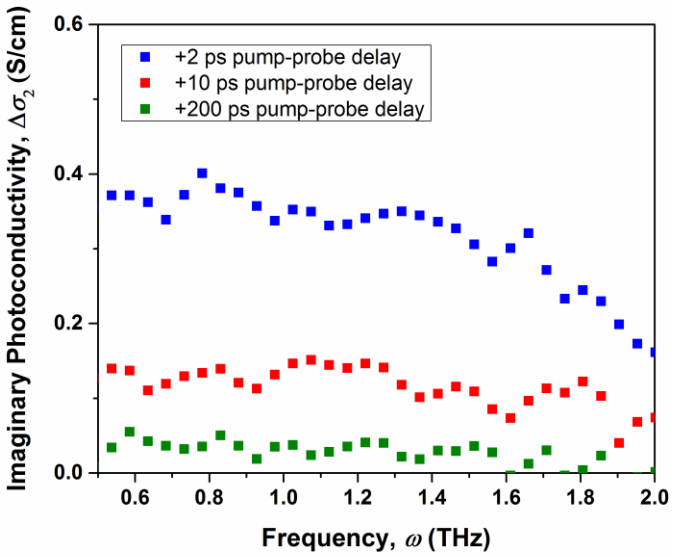

Figure S39. Frequency-dependence of the imaginary part of the THz photoconductivity collected from SnS nanoribbons at three different pump-probe delay times. The positive values of $\Delta\sigma_2$ (in addition to $\Delta\sigma_1$, see Fig. 8b) suggest Drude-like free carrier dynamics and scattering.

Scheme S~~21~~. Derivation of the terahertz mobility (μ_T) equation.

To determine the carrier mobility of our samples, start with equation 2, the thin film equation[7]:

$$\Delta\sigma(t_{\mathrm{pp}}) = -\left(\frac{\Delta E(t_{\mathrm{pp}})}{E_0}\right)\left(\frac{n_{\mathrm{THz}}+1}{Z_0 d}\right) \qquad (2)$$

Next, we consider the combined carrier DC conductivity equation for electrons and holes, $\sigma = e(n_{\mathrm{e}}\mu_{\mathrm{e}} + n_{\mathrm{h}}\mu_{\mathrm{h}})$, where *e* is the charge of an electron, *n* is the carrier concentration, and μ is the carrier mobility. If we assume that all free charge carriers are photogenerated by optical excitation in an equal ratio of electron-hole pairs, then $n_e = n_h = N$ and the DC photoconductivity is:

$$\sigma(t_{\mathrm{pp}}) = eN[\mu_{\mathrm{T}}(t_{\mathrm{pp}})] \qquad (S1)$$

where the terahertz mobility, μ_T, is equal to the sum of the carrier mobilities, ($\mu_e + \mu_h$). The charge carrier concentration resulting from photoexcitation was estimated according to:

$$N = \frac{\varphi FA}{d} \qquad (S2)$$

where φ is the charge carrier photogeneration efficiency, *F* is the excitation fluence in photons / cm^2, and the absorbance *A* is equal to (1-*R*-*T*), where *R* and *T* is the fraction of pump photon reflection and transmission, respectively. Combining Equation 2, Equation S1, and Equation S2 for a system where $\Delta\sigma(t_{pp})$ can be assumed $\approx \sigma(t_{pp})$ (see Figure S37), we find the time-dependent terahertz mobility (Equation 3 in the main text):

$$\mu_T(t_{\mathrm{pp}}) = -\left(\frac{\Delta E(t_{\mathrm{pp}})}{E_0}\right)\left(\frac{n_{\mathrm{THz}}+1}{Z_0 e\varphi FA}\right) \qquad (3)$$

Scheme S32. Derivation of the approx. relationship between μ_e and μ_h with μ_T in TRTS.

We propose the following scheme to approximate the deconvolution of a 2D materials' individual carrier mobilities, $\mu_{e,xy}$ and $\mu_{h,xy}$, from the TRTS-measured μ_T.

According to the Drude model, the drift mobility of a carrier, μ, can be expressed in terms of the scattering time, τ, and the effective mass, m^*:

$$\mu = \frac{e\tau}{m^*} \tag{S3}$$

At room temperature, carrier scattering is primarily due to lattice (aka phonon) scattering, as opposed to impurity scattering. Derived from Fermi's Golden Rule, the acoustic phonon-limited momentum scattering time for 2D and layered materials is:[8-10]

$$\tau = \frac{\hbar^3 \rho v_s^2}{m_{xy}^* E_d^2 k_B T} \tag{S4}$$

where ρ is mass density, v_s is longitudinal sound velocity, T is temperature, E_d is the composite deformation potential, and m^*_{xy} is the composite of the 2D in-plane directions. This approximation assumes photoinduced current primarily in the in-plane directions, and the model is valid only when transport is substantially less favorable in the out-of-plane direction. Combining S3 and S4 gives the in-plane carrier mobility as:

$$\mu_{xy} = \frac{e\frac{\hbar^3 \rho v_s^2}{m_{xy}^* E_d^2 k_B T}}{m_{xy}^*} = \frac{e\hbar^3 \rho v_s^2}{(m_{xy}^*)^2 E_d^2 k_B T} = A\left(\frac{1}{m_{xy}^* E_d}\right)^2 \tag{S5}$$

where A is a set of carrier-independent constants for a given 2D material at a steady state temperature. Therefore, the relationship between $\mu_{e,xy}$ and $\mu_{h,xy}$ can be expressed:

$$\frac{\mu_{e,xy}}{\mu_{h,xy}} = \frac{A\left(\frac{1}{m_{e,xy}^* E_{d,e}}\right)^2}{A\left(\frac{1}{m_{h,xy}^* E_{d,h}}\right)^2}$$

oOr:

$$\mu_{e,xy} = \mu_{h,xy}\left(\frac{m_{h,xy}^* E_{d,h}}{m_{e,xy}^* E_{d,e}}\right)^2 \quad \text{and} \quad \mu_{h,xy} = \mu_{e,xy}\left(\frac{m_{e,xy}^* E_{d,e}}{m_{h,xy}^* E_{d,h}}\right)^2 \tag{S6}$$

which we take as an approximation of the collective in-plane carrier mobility in terms of the in-plane mobility of the complimentary carrier for a 2D or layered material. This can then be combined with the TRTS mobility relation $\mu_e + \mu_h = \mu_T$ to yield:

$$\mu_{h,xy} = \frac{\mu_T}{1+\left(\frac{m_{h,xy}^* E_{d,h}}{m_{e,xy}^* E_{d,e}}\right)^2} \quad \text{and} \quad \mu_{e,xy} = \frac{\mu_T}{1+\left(\frac{m_{e,xy}^* E_{d,e}}{m_{h,xy}^* E_{d,h}}\right)^2} \tag{4}$$

which is an estimation of the mobility of individual carriers in terms of μ_T, E_d, and m^*_{xy}. Note that the resultant carrier mobility has contribution from multiple in-plane directions

unless μ_T was collected with a polarized TRTS measurement on a single crystal. In that case, values of E_d and m^* correspond to the investigated crystallographic orientation.

Scheme S43. Calculation of TRTS-measured independent carrier mobilities for SnS nanoribbons and square nanosheets.

m^* and E_d for α-SnS were tabulated from a variety of reports to provide a consensus calculation from first principles.[10-14] After calculating the geometric mean from the direction-dependent values, we used the following parameters in our analysis:
$m^*_{h,xy} = 0.26m_0$ $m^*_{e,xy} = 0.17m_0$ $E_{d,h} = 18.4$ eV $E_{d,e} = 13.2$ eV

The values of μ_T obtained from TRTS at t_{pp} = 10 ps were μ_T = 26.5 cm^2/V·s for the SnS nanoribbons and μ_T = 158.0 cm^2/V·s for the square nanosheets (assuming $\varphi = 1$).

Employing Equation 4, this gives the following in-plane carrier mobilities:

SnS nanoribbons:	$\mu_{h,xy}$ = 4.8 cm^2 / V·s	$\mu_{e,xy}$ = 22 cm^2 / V·s
SnS square nanosheets:	$\mu_{h,xy}$ = 29 cm^2 / V·s	$\mu_{e,xy}$ = 130 cm^2 / V·s

Scheme S54. A method for approximating the direction-dependent carrier mobilities μ_x and μ_y from the in-plane carrier mobility μ_{xy}.

The transport direction-dependent variation of Equation S5, the carrier mobility equation for either electrons or holes in 2D or layered materials, is:

$$\mu_x = \frac{e\hbar^3\rho v_s^2}{m_x^* m_{xy}^* E_{d,x} E_{d,xy} k_B T} = A\frac{1}{m_x^* m_{xy}^* E_{d,x} E_{d,xy}} \qquad \text{(S7)}$$

where A is a set of carrier-independent constants for a given 2D material at a steady state temperature. Therefore, the relationship between $\mu_{e,x}$ and $\mu_{e,y}$ can be expressed:

$$\frac{\mu_{e,x}}{\mu_{e,y}} = \frac{A\frac{1}{m_{e,x}^* m_{e,xy}^* E_{d,e,x} E_{d,e,xy}}}{A\frac{1}{m_{e,y}^* m_{e,xy}^* E_{d,e,y} E_{d,e,xy}}}$$

Or:

$$\mu_{e,x} = \mu_{e,y}\left(\frac{m_{e,y}^* E_{d,e,y}}{m_{e,x}^* E_{d,e,x}}\right) \text{ and } \mu_{e,y} = \mu_{e,x}\left(\frac{m_{e,x}^* E_{d,e,x}}{m_{e,y}^* E_{d,e,y}}\right) \qquad \text{(S8)}$$

and likewise for hole mobility. Assuming that the direction-specific carrier mobilities can be estimated from the composite in-plane mobility using a geometric mean, where $\mu_{xy} = \sqrt{\mu_x \mu_y}$, then we propose:

$$\mu_x = \sqrt{\left(\frac{m_x^* E_{d,x}}{m_y^* E_{d,y}}\right)}\mu_{xy} \quad \text{and} \quad \mu_y = \sqrt{\left(\frac{m_y^* E_{d,y}}{m_x^* E_{d,x}}\right)}\mu_{xy} \qquad (5)$$

where values of μ, m^*, and E_d are all carrier-dependent.

Scheme S5. Calculation of TRTS-measured direction-dependent carrier mobilities μ_x and μ_y from the in-plane mobility μ_{xy}.

Direction-dependent values of m^* and E_d for α-SnS were taken from Guo, *et al.*[10]:

$m^*_{h,zigzag} = 0.21m_0$ $m^*_{e,zigzag} = 0.15m_0$ $E_{d,h,zigzag} = 21.9$ eV $E_{d,e,zigzag} = 11.0$ eV

$m^*_{h,armchair} = 0.36m_0$ $m^*_{e,armchair} = 0.20m_0$ $E_{d,h,armchair} = 19.1$ eV $E_{d,e,armchair} = 14.6$ eV

Using Equation 5 and the values of $\mu_{h,xy}$ and $\mu_{e,xy}$ previously extracted from TRTS data, we approximate direction-dependent carrier mobilities in our 2D SnS nanocrystals:

SnS nanoribbons:	$\mu_{h,zigzag}$ = 5.8 cm^2 / V·s	$\mu_{e,zigzag}$ = 29 cm^2 / V·s
	$\mu_{h,armchair}$ = 3.9 cm^2 / V·s	$\mu_{e,armchair}$ = 16 cm^2 / V·s
SnS square nanosheets:	$\mu_{h,zigzag}$ = 35 cm^2 / V·s	$\mu_{e,zigzag}$ = 170 cm^2 / V·s
	$\mu_{h,armchair}$ = 23 cm^2 / V·s	$\mu_{e,armchair}$ = 97 cm^2 / V·s

Table S1. Reported electronic transport properties for undoped SnS at room temperature collected from various references. (NR = not reported)

Reference Number	Synthesis	Structure	Conductivity (S / cm)	Majority carrier	Hall mobility (cm^2 / V·s)	Carrier concentration (cm^{-3})
15	PVD	Single crystal	0.0083	h^+	34	1.52 x 10^{15}
16	Bridgman-Stockbarger	Single crystal	2.08	h^+	65	2 x 10^{17}
17	Bridgman-Stockbarger	Single crystal	NR	h^+	90	4 x 10^{17}
18	Bridgman-Stockbarger	Single crystal	0.019	h^+	48	2.68 x 10^{15}
19	Bridgman-Stockbarger	Single crystal	0.193	h^+	NR	5.07 x 10^{13}
20	Exfoliation	Single crystal	NR	h^+	10 - 25	4.0 x 10^{11}
21	Solution synthesis	Dropcast films of crystals	0.93	h^+	5.7	1 x 10^{18}
22	Spray pyrolysis	Polycrystalline thin film	0.033	e^-	130	1.6 x 10^{15}
23	Vacuum evaporation	Polycrystalline thin film	0.05-0.077	h^+	400 - 500	6.3 x 10^{14} - 1.2 x 10^{15}
24	ALD	Polycrystalline thin film	0.0014 - 0.017	h^+	0.82 - 15.3	6.9 x 10^{15} - 1.5 x 10^{16}
25	Pulsed laser deposition	Polycrystalline thin film	0.024	h^+	25 - 37	4 x 10^{15}
26	CVD	Polycrystalline thin film	0.001 - 0.01	h^+	3 - 10	10^{15} - 10^{16}
27	Thermal evaporation	Polycrystalline thin film	0.02 - 0.16	h^+	20.1 - 31.6	6.3 x 10^{15} - 3.1 x 10^{16}
28	CVT	Polycrystalline thin film	0.069	h^+	3.73	1.16 x 10^{17}

29	Vacuum evaporation	Polycrystalline thin film	0.008 - 0.012	h^+	0.8 - 31.6	1.7×10^{15} - 9.0×10^{16}

Supporting Information References.

(1.) Villars, P. *Pearson's Handbook Desk Edition: Crystallography Data for Intermetallic Phases*; ASM International: Materials Park, OH, 1998.

(2.) Biacchi, A. J.; Vaughn, D. D.; Schaak, R. E. Synthesis and Crystallographic Analysis of Shape-Controlled SnS Nanocrystal Photocatalysts: Evidence for a Pseudotetragonal Structural Modification. *J. Am. Chem. Soc.* **2013,** *135*, 11634-11644.

(3.) Whittles, T. J.; Burton, L. A.; Skelton, J. M.; Walsh, A.; Veal, T. D.; Dhanak, V. R. Band Alignments, Valence Bands, and Core Levels in the Tin Sulfides SnS, SnS2, and Sn2S3: Experiment and Theory. *Chem. Mater.* **2016**, *28*, 3718-3726.

(4.) NIST X-ray Photoelectron Spectroscopy Database. https://srdata.nist.gov/xps/Default.aspx (accessed October 26, 2017).

(5.) Tritsaris, G. A.; Malone, B. D.; Kaxiras, E. Structural stability and electronic properties of low-index surfaces of SnS. *J. Appl. Phys.* **2014**, *115*, 173702.

(6.) van der Pauw, L. J. A Method of Measuring Specific Resistivity and Hall Effect of Discs of Arbitrary Shape. *Philips Res. Rep.* **1958**, *13*, 1-9.

(7.) Hegmann, F. A.; Ostroverkhova, O.; Cooke, D. G., *Photophysics of Molecular Materials*. Wiley-VCH: Weinheim, 2006.

(8.) Li, S.-L.; Tsukagoshi, K.; Orgiu, E.; Samori, P. Charge Transport and Mobility Engineering in Two-Dimensional Transition Metal Chalcogenide Semiconductors. *Chem. Soc. Rev.* **2016**, *45*, 118-151.

(9.) Strait, J. H.; Nene, P.; Rana, F. High Intrinsic Mobility and Ultrafast Carrier Dynamics in Multilayer Metal-Dichalcogenide MoS_2. *Phys. Rev. B* **2014**, *90*, 245402.

(10.) Guo, R.; Wang, X.; Kuang, Y.; Huang, B. First-Principles Study of Anisotropic Thermoelectric Transport Properties of IV-VI Semiconductor Compounds SnSe and SnS. *Phys. Rev. B* **2015**, *92*, 115202.

(11.) Vidal, J.; Lany, S.; d'Avezac, M.; Zunger, A.; Zakutayev, A.; Francis, J.; Tate, J. Band-structure, Optical Properties, and Defect Physics of the Photovoltaic Semiconductor SnS. *Appl. Phys. Lett.* **2012**, *100*, 032104.

(12.) Xin, C.; Zheng, J.; Su, Y.; Li, S.; Zhang, B.; Feng, Y.; Pan, F. Few-Layer Tin Sulfide: A New Black-Phosphorus-Analogue 2D Material with a Sizeable Band

Gap, Odd–Even Quantum Confinement Effect, and High Carrier Mobility. *J. Phys. Chem. C* **2016**, *120*, 22663-22669.

(13.) Tritsaris, G. A.; Malone, B. D.; Kaxiras, E. Optoelectronic Properties of Single-Layer, Double-Layer, and Bulk Tin Sulfide: A Theoretical Study. *J. Appl. Phys.* **2013**, *113*, 233507.

(14.) Shafique, A.; Shin, Y.-H. Thermoelectric and Phonon Transport Properties of Two-Dimensional IV–VI Compounds. *Sci. Rep.* **2017**, *7*, 506.

(15.) Hegde, S. S.; Kunjomana, A. G.; Chandrasekharan, K. A.; Ramesh, K.; Prashantha, M. Optical and Electrical Properties of SnS Semiconductor Crystals Grown by Physical Vapor Deposition Technique. *Physica B* **2011**, *406*, 1143-1148.

(16.) Albers, W.; Haas, C.; van der Maesen, F. The Preparation and the Electrical and Optical Properties of SnS Crystals. *J. Phys. Chem. Solids* **1960**, *15*, 306-310.

(17.) Albers, W.; Haas, C.; Vink, H. J.; Wasscher, J. D. Investigations on SnS. *J. Appl. Phys.* **1961**, *32*, 2220-2225.

(18.) Patel, T. H.; Vaidya, R.; Patel, S. G. Growth and Transport Properties of Tin Monosulphoselenide Single Crystals. *J. Cryst. Growth* **2003**, *253*, 52-58.

(19.) Nassary. M. M. Temperature Dependence of the Electrical Conductivity, Hall Effect and Thermoelectric Power of SnS Single Crystals. *J. Alloys Compd.* **2005**, *398*, 21-25.

(20.) Sucharitakul, S.; Kumar, U. R.; Sankar, R.; Chou, F.-C.; Chen, Y.-T.; Wang, C.; He, C.; He, R.; Gao, X. P. A. Screening Limited Switching Performance of Multilayer 2D Semiconductor FETs: the Case for SnS. *Nanoscale* **2016**, *8*, 19050-19057.

(21.) Herron, S. M.; Tanskanen, J. T.; Roelofs, K. E.; Bent, S. F. Highly Textured Tin(II) Sulfide Thin Films Formed from Sheetlike Nanocrystal Inks. *Chem. Mater.* **2014**, *26*, 7106-7113.

(22.) Koteeswara Reddy, N.; Ramakrishna Reddy, K. T. Electrical Properties of Spray Pyrolytic Tin Sulfide Films. *Solid-State Electron.* **2005**, *49*, 902-906.

(23.) Noguchi, H.; Setiyadi, A.; Tanamura, H.; Nagatomo, T.; Omoto, O. Molecular Beam Epitaxy Growth of High Quality p-Doped SnS van der Waals Epitaxy on a Graphene Buffer Layer. *Sol. Energy Mater. Sol. Cells* **1994**, *35*, 325-331.

(24.) Sinsermsuksakul, P.; Heo, J.; Noh, W.; Hock, A. S.; Gordon, R. G. Atomic Layer Deposition of Tin Monosulfide Thin Films. *Adv. Energy Mater.* **2011**, *1*, 1116-1125.

(25.) Ran, F.-Y.; Xiao, Z.; Hiramatsu, H.; Hosono, H.; Kamiya, T. Growth of High-Quality SnS Epitaxial Films by H_2S Flow Pulsed Laser Deposition. *Appl. Phys. Lett.* **2014**, *104*, 072106.

(26.) Park, H. H.; Heasley, R.; Sun, L.; Steinmann, V.; Jaramillo, R.; Hartman, K.; Chakraborty, R.; Sinsermsuksakul, P.; Chua, D.; Buonassisi, T.; Gordon, R. G. Co-Optimization of SnS Absorber and Zn(O,S) Buffer Materials for Improved Solar Cells. *Prog. Photovoltaics* **2015,** *23,* 901-908.

(27.) Chakraborty, R.; Steinmann, V.; Mangan, N. M.; Brandt, R. E.; Poindexter, J. R.; Jaramillo, R.; Mailoa, J. P.; Hartman, K.; Polizzotti, A.; Yang, C.; Gordon, R. G.; Buonassisi, T. Non-Monotonic Effect of Growth Temperature on Carrier Collection in SnS Solar Cells. *Appl. Phys. Lett.* **2015**, *106*, 203901.

(28.) Hamzah, Y.; Guastavino, F.; Llinares, C.; Djessas, K.; Masse, G. SnS Thin Films Grown by Close-Spaced Vapor Transport. *J. Mater. Sci. Lett.* **2000**, *19*, 2135-2137.

(29.) Ghosh, B.; Bhattacharjee, R.; Banerjee, P.; Das, S. Structural and Optoelectronic Properties of Vacuum Evaporated SnS Thin Films Annealed in Argon Ambient. *Appl. Surf. Sci*. **2011**, *257*, 3670-3676.